2018 SCCS VALENCIA

UNIVERSITAT POLITÈCNICA DE VALÈNCIA

Proceedings of the 12th International Conference on Advances in Steel-Concrete Composite Structures

ASCCS 2018

27-29 June 2018, Universitat Politècnica de València, Spain

Scientific Editors

Vicente Albero
Ana Espinós
Carmen Ibáñez
Andrés Lapuebla
Manuel L. Romero

Congresos UPV
12th International Conference on Advances in Steel-Concrete Composite Structures (ASCCS 2018)
València, June 27-29, 2018

The contents of this publication have been evaluated by the Scientific Committee which it relates and the procedure set out http://ocs.editorial.upv.es/index.php/ASCCS/ASCCS2018/about/editorialPolicies

Vicente Albero
Ana Espinós
Carmen Ibáñez
Andrés Lapuebla
Manuel L. Romero

www.lalibreria.upv.es Ref.: 6384_10_01_01

ISBN: 978-84-9048-601-6

DOI: http://dx.doi.org/10.4995/ASCCS2018.2018.8534

PREFACE

The Association of Steel and Concrete Composite Structures (ASCCS) aims at contributing to the exchange of new developments in the field of steel-concrete composite structures emphasizing the international collaboration in this area.

After the success of the previous ASCCS conference series: Harbin (1985, 1988, 2006), Fukuoka (1991), Kosice (1994), Innsbruck (1997), Los Angeles (2000), Sydney (2003), Leeds (2009), Singapore (2012) and Beijing (2015), the 12th international conference on 'Advances in Steel-Concrete Composite Structures' (ASCCS 2018) will be held by Universitat Politècnica de València, Spain on June 27-29, 2018.

The general topics are focussed on different subjects such as beams, slabs, columns, connections, applications, case studies and new materials, earthquake, fatigue and dynamic response, design and standard developments, fire resistance, impact, blast and robustness.

In addition, twelve keynote speakers will give their vision on the recent progress and advances in the research, design and practice of steel-concrete composite as well as hybrid structures.

This book contains the proceedings of the conference where more than 209 abstracts were received. All papers were internationally peer-reviewed and eventually 123 papers from 24 countries were accepted for publication. Selected papers will be published on a special issue of *Structures*, a joint international journal launched by the Institution of Structural Engineers and Elsevier.

I would like to express my gratitude to the members of International Scientific Committee for reviewing the papers and for the promotion of the conference. Thanks are due to all the conference chairs, speakers and all the participants whose support to the conference was essential to its success.

Special thanks are owed for making this conference possible to Vicente Albero, Ana Espinós, Carmen Ibañez and Andrés Lapuebla for their tireless effort maintaining the good work atmosphere despite the numerous problems occurred during last months.

Finally, support by the Universitat Politècnica de València is gratefully acknowledged.

Prof Manuel L. Romero
Chair of the Organizing Committee of ASCCS2018
Universitat Politècnica de València

COMMITTEES

LOCAL ORGANIZING COMMITTEE

Prof. Manuel L. Romero, Spain (*Chair of the local committee*)
Dr A. Espinós, Spain
Dr C. Ibáñez, Spain
Dr A. Lapuebla, Spain
Dr V. Albero, Spain

INTERNATIONAL SCIENTIFIC COMMITTEE

Frans Bijlaard, Netherlands
Reidar Bjorhovde, USA
Ian Burgess, UK
Dinar Camotim, Portugal
SL Chan, Hong Kong, China
Tak-Ming Chan, Hong Kong, China
SP Chiew, Singapore
KF Chung, Hong Kong, China
George Charles Clifton, N. Zealand
Luis S. da Silva, Portugal
Jean-Francois Demonceau, Belgium
Dan Dubina, Romania
WS Easterling, USA
Sherif El-Tawil, USA
Leroy Gardner, UK
Y Goto, Japan
Lin-Hai Han, China
Jerome F. Hajjar
Amin Heidarpour, Australia
Mohammed Hjiaj, France
Bassam A Izzudin, UK
SA Jayachandran, India
Venkatesh Kodur, USA
Ulrike Kuhlmann, Germany
Dennis Lam, UK
Roberto T Leon, USA
JYR Liew, Singapore
Judy Liu, USA
M Mahendran, Australia
David A Nethercot, UK
JA Packer, Canada
RJ Plank, UK
K Rasmussen, Australia
Z Tao, Australia
KH Tan, Singapore
JG Teng, Hong Kong, China
Chia Ming Uang, USA
Brian Uy, Australia
Frantisek Wald, Czech Republic
Yong Wang, UK
J Wardenier, Netherlands
Y Xiao, USA
Ben Young, Hong Kong, China
R Zandonini, Italy
Xiao Ling Zhao, Australia
A Zingoni, South Africa

ORGANIZING INSTITUTIONS

UNIVERSITAT POLITÈCNICA DE VALÈNCIA

ASCCS
Association for Steel-Concrete Composite Structures

INDEX

KEYNOTE LECTURES

Concrete-encased CFST structures: behaviour and application 1
L. H. Han, D. Y. Ma and K. Zhou

Finite element analysis of concrete filled lean duplex stainless steel columns 11
D. Lam, J. Yang, and X.H. Dai

Simplified numerical modelling of rectangular concrete-filled steel columns, beams and beam-columns 19
Z. Tao, U. Katwal, M. K. Hassa and W. D. Wang

Behaviour of steel and composite beam-column joints subjected to quasi-static and impact loads 29
K. Chen, K. H. Tan

Fatigue of steel bridges 39
U. Kuhlmann, S. Bove, S. Breunig and K. Drebenstedt

Steel Concrete Composite Systems for Modular Construction of High-rise Buildings 59
J. Y. R. Liew, Z. Dai and Y. S. Chua

Deformation based design of steel and composite structural elements 67
L. Gardner and X. Yun

Second-order direct analysis of steel structures made of tapered members 75
S.L. Chan, S.W. Liu and Y.P. Liu

Post-fire mechanical properties of high strength steels 83
H. T. Li and B. Young

Applications, behaviour and construction of high performance steels in steel-concrete composite structures 91
B. Uy

BEAMS/SLABS

Push-Out tests for a novel prefabricated steel-concrete composite shallow flooring system 101
I.M. Ahmed, K.D. Tsavdaridis, F. Neysari and J.P. Forth

Experimental study on mechanical performance of partially precast steel reinforced concrete beams 107
Yong Yang, Yicong Xue, Yunlong Yu and Ruyue Liu

Experimental study on demountable shear connectors in profiled composite slabs 115
J. Yang, D. Lam, X.H. Dai and T. Sheehan

Experimental study of steel-concrete composite beams comprised of fly ash based Geopolymer concrete 123
Balbir Singh, Ee Loon Tan, Zhu Pan, Olivia Mirza and Julius Boncato

Minimum degree of shear connection in composite beams in buildings 129
E. S. Aggelopoulos, G. H. Couchman and R. M. Lawson

Flexural behaviour of composite slim floor beams 137
T. Sheehan, X. Dai, J. Yang, K. Zhou and D. Lam

Bending moment capacity of stainless steel-concrete composite beams 145
R. Shamass, K.A. Cashell

Shear connection requirements for composite cellular beams 153
E. S. Aggelopoulos, F. Hanus and R.M. Lawson

Flexural behavior of steel-concrete composite beams with U-shaped steel girders 161
Y. Liu, L.H. Guo, and Z.G. Li

A novel one-sided push-out test for shear connectors in composite beams 169
M. A. Al-Shuwaili, A. Palmeri, M. Lombardo

Strut-and-tie model for the support of steel beams crossing concrete beams 177
F. Marie and H. Somja

The influence of vertical shear on the hogging bending moment resistance of ComFlor composite slabs 183
R. Abspoel, J.W.B. Stark and H.-J. Prins

Design for deconstruction for sustainable composite steel-concrete floor systems 191
L. Wang, M. D. Webster and J. F. Hajjar

Experimental analysis of composite push test integrating geopolymer concrete 199
Balbir Singh, Ee Loon Tan, Zhu Pan, Olivia Mirza and Youtam Mamo

Experimental investigations on built-up cold-formed steel beams connected by resistance spot welding 205
V. Ungureanu, I. Both, M. Burca, M. Grosan, C. Neagu and D. Dubina

Second-order flexibility-based model for nonlinear inelastic analysis of composite steel-concrete frameworks with partial composite action and semi-rigid connections 213
C.G. Chiorean, S.M. Buru

Horizontal push out tests on a steel-yielding demountable shear connector 221
E. Feidaki, G. Vasdravellis

Numerical evaluation of the plastic hinges developed in headed stud shear connectors in composite beams with profiled steel sheeting 229
V. Vigneri, C. Odenbreit, M. Braun

Design value of a headed stud shear resistance in composite steel – concrete beams – probability-based approach to evaluation 237
M. Maslak and T. Domanski

COLUMNS

Analysis and behavior of high-strength rectangular CFT columns 245
Z. Lai and A. H. Varma

Influence of steel tube thickness and concrete strength on the axial capacity of stub CFST columns 253
C. Ibañez, D. Hernández-Figueirido and A. Piquer

Finite element analysis of mechanical behavior of concrete-filled square steel tube short columns with inner I-shaped CFRP profiles subjected to bi-axial eccentric load 259
G. Li, Z. Zhan, Z. Yang, Y. Yang

Mega columns with several reinforced steel profiles – experimental and numerical investigations 267
T. Bogdan and M. Chrzanowski

Concrete-filled round-ended steel tubular stub columns under concentric and eccentric loads 275
A. Piquer, D. Hernández-Figueirido and C. Ibañez

Cooperative work behavior of high strength concrete-filled square high strength tubular stub columns with inner I-shaped CFRP under axial compression 281
G. Li, Y. Yang, Z. Yang and Z. Zhan

Behavior of innovative T-shaped multi-partition steel-concrete composite columns under concentric and eccentric compressive loadings 289
J. Chen, S.M. Zhang, Z.F. Huang, X.X. Zhang and L.H. Guo

Finite element analysis of concrete-encased steel composite columns with off-center steel section 297
B.L. Lai, J. Y. Richard Liew, S. Li

Compressive performance of 50 MPa strength concrete-filled square and circular tube (CFT) columns using recycled aggregate 305
S-M. Choi, W-H. Choi, K. Lee, J-Y. Ryoo, S. Kim and Y-P. Park

Experimental study of the force transfer mechanism in transition zone between composite column and reinforced concrete column 315
D. A. Dragan, A. Plumier and H. Degee

Experimental behaviour of very high-strength concrete-encased steel composite column subjected to axial compression and end moment 323
Z. Huang, X. Huang, W. Li, Y. Zhou, L. Sui and J. Y. Richard Liew

Comparison investigation on the load capacity of octagonal, circular and square concrete filled steel tubes 331
J-Y. Zhu and T-M. Chan

Numerical investigation on slender concrete-filled steel tubular columns subjected to biaxial bending 337
A. Espinós, V. Albero, M. L. Romero, M. Mund, I. Kleiboemer, P. Meyer and P. Schaumann

Numerical study of concrete-filled austenitic stainless steel CHS stub columns with high-strength steel inner tubes 343
F. Wang, B. Young and L. Gardner

Compressive behaviour of steel tubes filled with strain hardening cementitious composites 351
R. A. Shuaibu, Z. Tao, Z. Pan, M. K. Hassan and J. Zhou

Axial behaviour of concrete filled steel tube stub columns: a review 359
S. Guler, F. Korkut, N. Yaltay and D. Yavuz

Numerical analysis of concrete-filled spiral welded stainless steel tubes subjected to compression 365
D. Li, B. Uy, F. Aslani and C. Hou

Analytical behavior of concrete-filled aluminum tubular stub columns under axial compression 373
H-Y. Zhao, F-C. Wang, L-H. Han

Tests on sea sand concrete-filled stainless steel tubular stub columns 379
F.Y. Liao, C. Hou, W.J. Zhang and J. Ren

Experimental investigation on the bamboo-concrete filled circular steel tubular stub columns 385
D. Gan, T. Zhang, X. Zhou and Z. He

Direct plastic analysis of steel structures by flexibility-based element with initial imperfection 393
Y. Liu, G. P. Shu and S-L. Chan

Analytical behaviour of concrete-encased CFST box stub columns under axial compression 401
J. Y. Chen, L. H. Han, F. C. Wang and T. M. Mu

A numerical model with varying passive confinement for circular and elliptical concrete-filled steel tubular columns 409
C. D. Lacuesta, M. L. Romero, A. Lapuebla-Ferri and J. M. Adam

Investigations on global buckling behaviour of concrete-filled double-skinned steel tubular columns 419
U. M. Sulthana, S. A. Jayachandran

CONNECTIONS

Development of an innovative type of shear connector dedicated to fully embedded steel-concrete composite columns – experimental and numerical investigations 427
M. Chrzanowski, C. Odenbreit, R. Obiala, T. Bogdan, M. Braun and H. Degée

Headed studs close to the concrete edge under pull-out 435
A. M. Pascual, U. Kuhlmann, J. Ruopp and L. Stempniewski

Pull-out behaviour of extended hollobolts for hollow beam-column connections 441
M. F. Shamsudin and W. Tizani

Square reinforced CFST column to RC beam joint subjected to lateral loading: An investigation using finite element analysis 449
Zheng Zhou, Dan Gan, Xuhong Zhou, Kang Hai Tan

Improvement of bearing failure behaviour of T-shaped steel beam-reinforced concrete columns joints using perfbond plate connectors 457
Mikihito Yoshida and Yasushi Nishimura

Proposal of strength formula and type development of composite mega column to beam connections with T-shaped stiffener 465
Jae-Hyun Lee, Sun-Hee Kim, Bu-Kyu Kim, Kyong-Soo Yom and Sung-Mo Choi

Use of bolted shear connectors in composite construction 475
X. Dai, D. Lam, T. Sheehan, J. Yang and K. Zhou

Design of concrete-filled high strength steel tubular X-joints subjected to compression 483
H. T. Li and B. Young

Improvement of bearing performance on exterior steel beam-reinforced concrete column joints with steel columns 491
Shinya Nakaue, Yasushi Nishimura

Characterization and optimization of the steel beam to RC wall connection for use in innovative hybrid coupled wall systems 499
R. Das, H. Degee

Analysis of slab-column connections in CFT sections without continuity of the tube 507
A. Albareda-Valls, C. Milan, J. Maristany Carreras and D. Garcia Carrera

Characterisation of beam-to-column joints beyond current Eurocode provisions 513
J.-F. Demonceau and A. Ciutina

Analysis of fracture behavior of large steel beam-column connections 521
Liangjie Qi, Jonathan Paquette, Matthew Eatherton, Roberto Leon, Teodora Bogdan, Nicoleta Popa and Edurne Nunez Moreno

Experimental study on behavior of shear connectors embedded in steel-reinforced concrete joints 527
R.Nakamori, Y.Kageyama, and N. Baba

A new method to assess the stiffness and rotation capacity of composite joints 533
J. Duarte da Costa, R. Obiala and C. Odenbreit

Axially loaded grouted connections in offshore conditions using ordinary portland cement 541
P. Schaumann, J. Henneberg and A. Raba

Push-out tests on demountable shear connectors of steel-concrete composite structures 549
A. Kozma, C. Odenbreit, M.V. Braun, M. Veljkovic and M.P. Nijgh

Numerical behaviour of composite K-joints subjected to combined loading and corrosive environment 557
S. Saleh, C. Hou, L.H. Han, Y.X. Hua

Influence of joint rigidity on the elastic buckling load on sway and non-sway steel frames 565
A. N.T. Ihaddoudène, M. Saidani, and J. P. Jaspart

Punching shear based design of concrete-filled CHS T-Joints under in-plane bending 573
F. Xu, T.M. Chan and J. Chen

Push-out tests on embedded shear connections for hybrid girders with trapezoidal web 581
B. Jáger, G. Németh, N. Kovács, B. Kövesdi, M. Kachichian

Semi-continous beam-to-column joints for slim-floor systems in seismic zones 587
C. Vulcu, R. Don and A. Ciutina

Experimental investigation of two-bolt connections for high strength steel members 595
Yan-Bo Wang, Yi-Fan Lyu and Guo-Qiang Li

Deconstructable flush end plate beam-to-column composite joints: component-based modelling 601
M. A. Bradford, A. Ataei and X. Liu

APPLICATIONS, CASE STUDIES AND NEW MATERIALS

Sustainable steel and composite constructions for multifunctional commercial buildings 609
R. Stroetmann, L. Hüttig

An innovative concrete-steel structural system allowing for a fast and simple erection 617
C. Lepourry, H. Somja, P. Keo, P. Heng and F. Palas

Driving factors and obstacles in adopting structural steel in Hong Kong: Case studies 625
Y. Yang and A. P. C. Chan

Behaviour and design of composite steel and precast concrete transom for railway bridges application 633
O. Mirza, A. Talos, M. Hennessy and B. Kirkland

Study on non-buckling steel plate shear walls with corrugated core panel 639
H. J. Jin, G.Q. Li and F.F. Sun

Cylinders with a steel-concrete-steel wall to resist external pressure 647
C. D. Goode and T. Nash

Research progress on material properties of clad steel 653
H. Y. Ban, R. S. Bai, K. F. Chung, J. C. Zhu and Y. Bai

Toughness of old mild steels 659
R. M. Stroetmann, L. Sieber

Numerical study on the effect of welding and heating treatments on strength of high strength steel column 667
J. Jiang, W. Bao, J. Liu and Z.Y. Peng

Failure mechanism of foam concrete with C-Channel embedment 675
D. Liu, F. Wang and F. Fu

EARTHQUAKE, FATIGUE AND DYNAMIC RESPONSE

Seismic performance assessment of conventional steel and steel-concrete composite moment frames using CFST columns 685
A. Silva, Y. Jiang, L. Macedo, J.M. Castro and R. Monteiro

Simplified modelling of circular CFST members with a Concentrated Plasticity approach 693
Y. Jiang, A. Silva, L. Macedo, J.M. Castro, R. Monteiro and T.M. Chan

Performances of moment resisting frames with slender composite sections in low-to-moderate seismic areas 701
H. Degée, Y. Duchêne and B. Hoffmeister

Resistance of a steel-concrete hybrid thermal break system to low cycle fatigue under thermal actions 709
B. Le Gac, P. Keo, H. Somja and F. Palas

Hysteretic performance research on high strength circular concrete-filled thin-walled steel tubular columns 717
Jiantao Wang, Qing Sun

Fatigue and crack propagation investigations on composite dowels using an inclined single push-out test 725
K. Wolters, M. Feldmann

Experimental comparison study on cyclic behavior of coupled shear walls with steel and RC coupling beam 733
Mengde Pang, Guoqiang Li, Feifei Sun, Liulian Li and Jianyun Sun

Fragility curves for special truss moment frame with single and multiple vierendeel special segment 739
R. Kumar, D. R. Sahoo and A. Gupta

DESIGN AND STANDARD DEVELOPMENTS

The SMARTCOCO design guide for hybrid concrete-steel structures 749
H. Somja, M. Hjiaj, Q.H. Nguyen, A. Plumier and H. Degee

Design of composite columns based on Eurocode - Comparison between general and simplified methods 757
H. Unterweger, M. Kettler

Composite column tests – database and comparison with Eurocode 4 763
C. D. Goode

Comparison of design for composite columns in steel and concrete according to Eurocode 4 and Chinese design codes 769
Q. Zhang, M. Schäfer

FIRE RESISTANCE

Fire performance of concrete-encased CFST columns and beam-column joints 779
K. Zhou and L.H. Han

Fire and post-fire performance of circular steel tube confined reinforced concrete columns 787
F. Liu, H. Yang, and S. Zhang

Analysis of concrete-filled steel tubular columns after fire exposure 795
C. Ibañez, L. Bisby, D. Rush, M. L. Romero, A. Hospitaler

Behavior of concrete-filled double skin steel tubular columns under eccentric compression after fire 803
X. Liu, J. Y. Xu and B. Wang

Experimental investigations on the load-bearing behaviour of an innovative prestressed composite floor system in fire 811
P. Schaumann, P. Meyer, M. Mensinger and S. K. Koh

Experimental study on the thermal behaviour of fire exposed slim-floor beams 819
V. Albero, A. Espinós, E. Serra, M. L. Romero and A. Hospitaler

Analysis of concrete-filled stainless steel tubular columns under combined fire and loading 825
Q. H. Tan, L. Gardner, L. H. Han and D. Y. Song

The effect of damage location on the performance of seismically damaged concrete filled steel tube columns at fire 835
E. Talebi, M. Korzen, A. Espinós, and S. Hothan

Finite element analysis of the flexural behavior of square CFST beams at ambient and elevated temperature 843
M. F. Javed, N. H. Ramli Sulong, N.B. Khan, S. Kashif

Material tests of 316L austenitic stainless-clad steel at elevated temperatures 851
R. S. Bai, H. Y. Ban, K. F. Chung and Yin Bai

Experimental study on spalling risk of concrete with 115~120MPa subject to ISO834 Fire 857
Y. Du, Y. Zhu and J. Y. R. Liew

To shear failure of steel and fibre-reinforced concrete circular hollow section composite column at elevated temperature 863
T. Arha, V. Křístek, A. Tretyakov, L. Blesák, I. Tkalenko,F. Wald, R. Stefan, J. Novak and A. Kohoutková

IMPACT, BLAST AND ROBUSTNESS

Factors affecting the response of steel columns to close-in detonations 873
F. Dinu, I. Marginean, D. Dubina, A. Khalil and E. De Iuliis

Experimental study on in-plane capacities of composite steel-concrete floor 881
P. Heng, H. Somja, and M. Hjiaj

The effect of composite floor on the robustness of a steel self-centering MRF under column loss 889
C.A. Dimopoulos, F. Freddi, T.L. Karavasilis and G. Vasdravellis

Numerical study on steel-concrete composite floor systems under corner column removal scenario 897
Qiu Ni Fu and K. H. Tan

An experimental study of composite effect on the behaviour of beam-column joints subjected to impact load 905
K. Chen, K. H. Tan

Robustness of prefabricated prefinished volumetric construction (PPVC) high-rise building 913
Y. S. Chua, J. Y. R. Liew and S. D. Pang

AUTHOR INDEX 921

KEYNOTE LECTURES

12th International Conference on Advances in Steel-Concrete Composite Structures (ASCCS 2018)
Universitat Politècnica de València, València, Spain, June 27-29, 2018
Doi: http://dx.doi.org/10.4995/ASCCS2018.2018.7109

Concrete-encased CFST structures: behaviour and application

L. H. Han[a]*, D. Y. Ma[a] and K. Zhou[a]

[a]Department of Civil Engineering, Tsinghua University, China
*corresponding author, e-mail address: lhhan@mail.tsinghua.edu.cn

Abstract

Concrete-encased CFST (concrete-filled steel tube) is a kind of composite structure comprised of a CFST component and a reinforced concrete (RC) component. The concrete encased CFST possesses superior ductility and higher stiffness. They are gaining popularity in high-rise buildings, large-span structures, bridges, subway stations and workshops. This paper initially reviews the recent research on concrete-encased CFST structures. The major research findings on bond performance, static performance, dynamic performance and fire resistance are presented. This paper also outlines some construction considerations, such as the utilization of materials, the fabrication of the steel tube, and the methods of casting the inner and outer concrete. Finally, some typical practical projects utilizing concrete-encased CFST members are presented and reviewed.

Keywords: *concrete-encased; concrete-filled steel tube (CFST); structural behaviour; composite action; construction.*

1. Introduction

Concrete-encased CFST (concrete-filled steel tubes) are a kind of composite member consisting of an inner CFST component and an outer reinforce concrete (RC) component as an encasement. These kinds of composite members are characterized by high earthquake resistance, superior ductility, high compressive strength, high shear strength and ease of construction. Five typical concrete-encased CFST sections popularly used in China are presented in Fig. 1. Steel tubes with different sections, such as circular section (CS), square section (SS) and rectangular section (RS), are used. They are usually aligned centrally with respect to the outer RC component. This kind of composite member was initially designed to achieve a good seismic performance by applying a greater load ratio on the inner CFST component and a lesser load ratio on the outer RC component, so that the outer RC component has high capacity of resisting compression when subjected to seismic action. It was first used in China in 1995 to improve steel reinforced concrete (SRC) structures. The idea of applying RC encasement to the outer is similar to SRC, which has also been also illustrated in Eurocode [1].

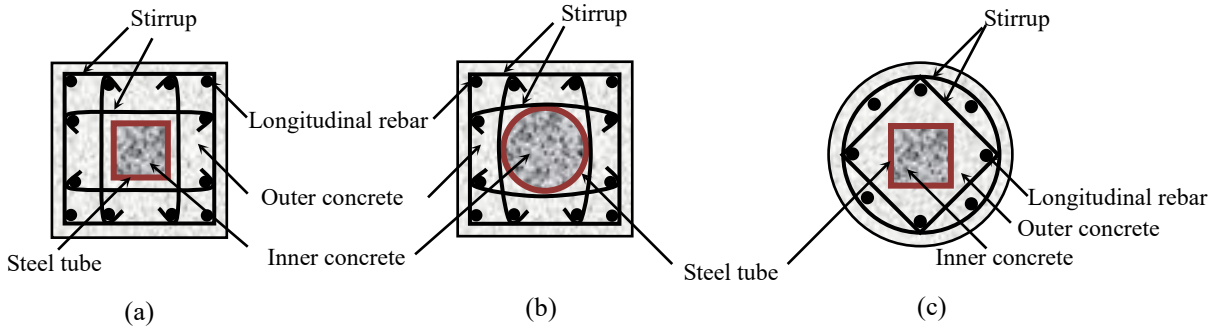

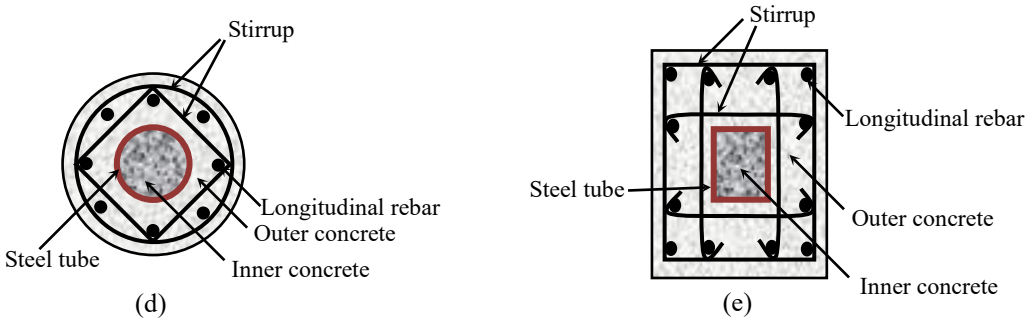

Fig. 1. Typical sections of the concrete-encased CFST.

Concrete-encased CFST also has some benefits in respect to construction. The inner steel tube is usually erected first, and it can serve as the support for the following construction. The concrete filled in the steel tube can be cast before the outer concrete or together with the outer concrete. The former and the latter methods are defined as the different-stage construction and the same-stage construction, respectively. Another benefit is that concrete-encased CFST column can be easily connected to RC beams. The configurations of the joint can be implemented based on the RC beam to RC column joints.

2. Behaviour of concrete-encased CFST members

Concrete-encased CFST structures can generally be classified by their structural functions: members, connections/joints and structural systems. The behaviour of each category has been studied in the past decade. The research purposes are to provide design recommendations, to promote practical applications and to lead to code coverage. Existing research on the performance of concrete-encased CFST structures is presented below, including bond performance, confinement effects, static performance, dynamic performance and fire performance.

2.1. Bond performance

Effective stress transfer between the steel tube and the outer concrete are required to ensure the composite action of the CFST component and the RC component. A series of tests have been carried out to investigate the bond performance of concrete-encased CFST columns by Han et al. [2]. The measured bond stress versus slip relationships of a CFST column with circular section [3] and a concrete-encased CFST column with circular steel hollow section [2] are compared in Fig. 2. It can be found that the bond strength of the concrete-encased CFST column is approximately triple that of the CFST column. It indicates that the composite action of the inner CFST component and the outer RC component can be well achieved without using additional shear connectors. Meanwhile, it is interesting to find that the bond stress versus slip relationships of the concrete-encased CFST column fluctuates dramatically, while that of the CFST column is smooth. To the authors' best knowledge, no publication is available on the bond performance of concrete-encased CFST column after fire. But the bond performance of CFST column after fire has been experimentally studied by Tao et al. [3], and the key influencing parameters were identified.

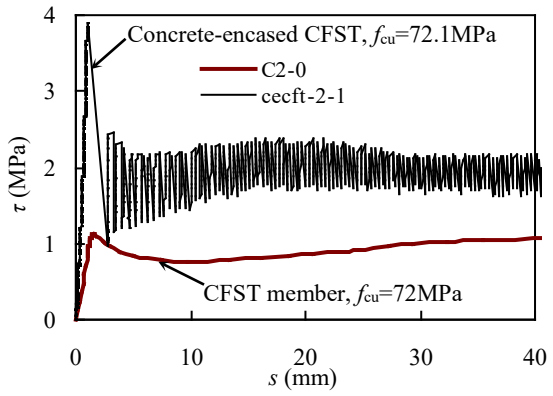

Fig. 2. Bond stress (τ) versus slip (s) relationships [2].

2.2. Confinement effects between the steel tube and the concrete

The confinement effects come from the structural interaction between the steel tube and the concrete. The confinement effects can improve the structural behaviour of the concrete-encased CFST structures.

The confinement effect between the steel and concrete components in CFST has been studied by many researchers [4]. It is believed that the confinement effect is related to the cross-sectional profile as well as the material properties. The confinement of concrete-encased CFST is not only between the steel tube and inner concrete, but also between the steel tube and outer concrete. The outer concrete can provide confinements to the steel tube, which can prevent the steel tube from early local buckling [5]. Moreover, the CFST component can sustain the load after the crushing of outer concrete, which is beneficial for the ductility of concrete-encased CFST members [6].

2.3. Static performance

The static performance includes the behaviour of concrete-encased CFST members under axial compression, axial tension, bending moment and eccentric loading. The existing experimental research of concrete-encased CFST stub column under axial compression load includes concrete-encased CFST columns with circular section (Fig. 1(d)) [7], square section (Fig. 1(b)) [5][8]. As reported by researchers, the failure modes of concrete-encased CFST stub columns are usually characterized by the mid-height crushing of outer concrete, as shown in Fig. 3(a). Furthermore, significant local buckling at mid-height longitudinal rebars can be observed as show in Fig. 3(b). By contrast, the steel tube kept intact after the test. In addition, due to the effective confinement of the steel tube, the concrete core is not crushed as shown in Fig. 3(c). It indicates that the inner CFST component becomes the main part supporting the load after the outer concrete crushes.

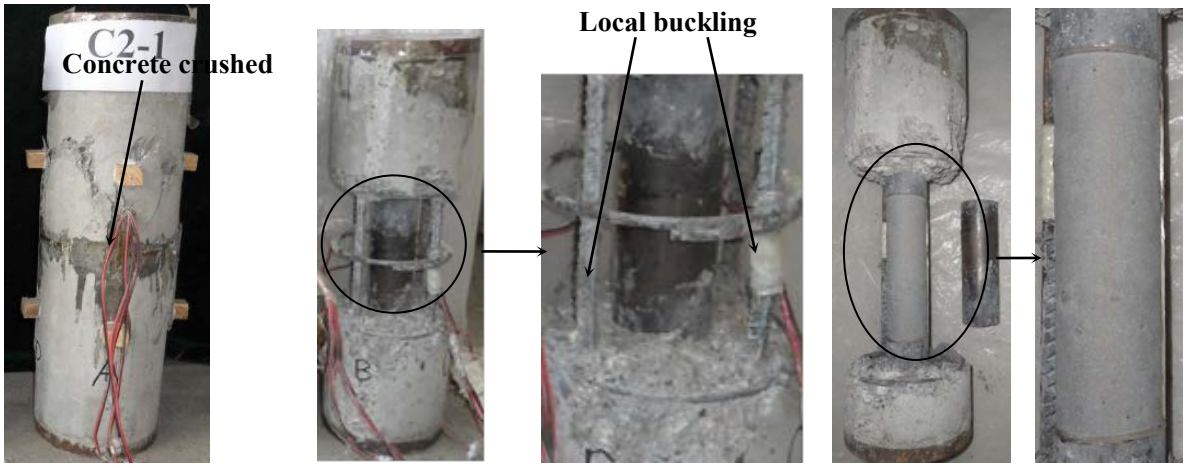

Fig. 3. Failure modes of typical concrete-encased CFST stub columns.

The axial compressive behaviour has also been investigated. Fig. 4 shows the measured load (N) versus axial deformation (Δ) relationships of a concrete-encased CFST stub column as well as that of its RC counterpart. The RC counterpart rc1-1 and rc1-2 have identical test parameters. It can be found that the load carrying capacity of the concrete-encased CFST stub column is 40.4% higher than that of its RC counterpart. Meanwhile, compared to its RC counterpart, the descent stage of N-Δ relationships of the concrete-encased CFST stub column is smoother. The deformation corresponding to the peak load is improved by 25.97%. This indicates that the concrete-encased CFST stub column possesses superior axial compressive strength and ductility than the RC stub column.

Theoretical studies on the concrete-encased CFST stub column under axial compressive loading are also available [4][5]. It can be found that the compressive strength of the concrete-encased CFST stub column is higher than the simple superposition of the compressive strength of each part, i.e., the longitudinal reinforcement, the outer concrete, the inner concrete and the steel tube.

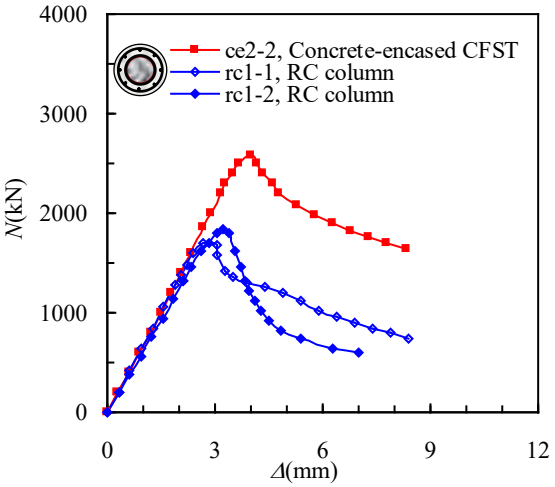

Fig. 4. Load (N) versus axial deformation (Δ) relationships of stub columns [7].

The bending behaviour of concrete-encased CFST beams with square section (Fig. 1(b)) was investigated by An et al. [9]. Three methods were used, i.e., experimental method, ultimate balance method and strap method. It should be noted that the steel tube has limited influence on the bending strength of concrete-encased CFST beams. The behaviour of concrete-encased CFST columns under eccentric loading has also been investigated. Various cross sections were studied, such as circular section (Fig. 1 (d)) [4] square section (Fig. 1 (b)) [9] and rectangular section (Fig. 1(e)) [11]. The measured load (N) versus axial deformation (Δ) relationships of a concrete-encased CFST beam-column are presented in Fig. 5. The strain corresponding to the ultimate strength of the concrete-encased CFST column exceeds that of the outer RC component by 23.0% due to the contribution of the inner CFST component.

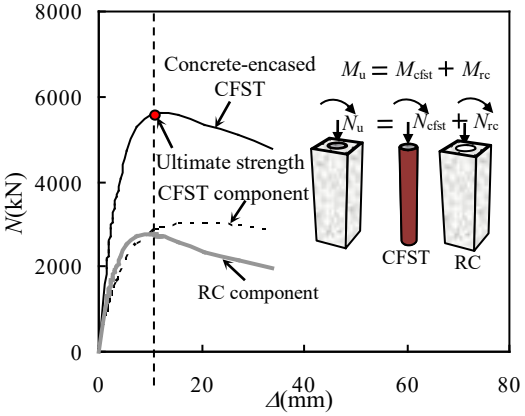

Fig. 5. Load (N) versus axial deformation (Δ) relationships of beam-columns [6].

2.4. Dynamic performance

As stated above, concrete-encased CFST members were initially designed to achieve a good seismic performance by applying a greater load ratio on the inner CFST component and a lesser load ratio on the outer RC component, so that the outer RC component has higher capacity of developing compression when subjected to seismic action. A large number of research work is available on the dynamic performance of the concrete-encased CFST member. The studies of dynamic behaviour include cyclic behaviour and impact behaviour.

Some experimental studies have been conducted on the cyclic behaviour of concrete-encased CFST beam-columns [12][13][14][15]. It can be found from these tests that concrete-encased CFST beam-columns exhibit favourable energy dissipation and ductility, even when they are subjected to high axial compression loads. The analytical research has been conducted by Qian et al. [16] and Ma et al. [17]. As recommended by Qian et al. [16], the concrete-encased CFST column exhibits good ductility performance under cyclic loading, where the curvature ductility coefficient can be 15% higher than the RC counterpart. It confirms that concrete-encased CFST column is suitable for application in regions of high seismicity [12].

The existing concrete-encased CFST joints include the concrete-encased CFST column to RC beam joint [18][19] and the concrete-encased CFST column to steel beam joint [4][19]. The test results indicate that both joints exhibit favourable energy dissipation and high shear strength. For the high shear and bending strength of a concrete-encased CFST column, the failure usually occurs at beam ends rather than at column ends or joint.

The studies on the impact behaviour of concrete-encased CFST beam-column are limited. Han et al. [20] conducted experimental studies on concrete-encased CFST beam-column. Compared to the RC counterpart, concrete-encased CFST beam-column exhibits an overall deformation under lateral impact. The major penetrating cracks, commonly observed in RC beam-columns, were not observed in concrete-encased CFST beam-column. This kind of beam-column shows ductile failure mode under lateral impact.

2.5. Fire performance

Experimental investigations have been conducted on the fire performance of concrete-encased CFST column. Ten tests were conducted, including six fire resistance tests and four postfire tests [21]. The specimens were subjected to a combined effect of both loading and fire, consisting of a loading phase at ambient temperature, a standard fire exposure phase, a cooling phase and postfire loading phase. The test parameters investigated were load ratio, dimension of steel tube and heating time ratio. Fig. 6 shows the failure modes of concrete-encased CFST after tests. The global buckling failure mode was observed for all tested specimens. Compared with fire resistance tests (Fig. 6 (a)), the failure modes of postfire tests (Fig. 6 (b)) exhibited more evident plastic hinges near mid-height and both ends. After the tests, the outer concrete was removed and the inner steel tubes were cut open at the locations where the lateral deflection peaked. The removal of outer concrete was tough, indicating that the reinforcement provided efficient confinement to the inner components after fire exposure.

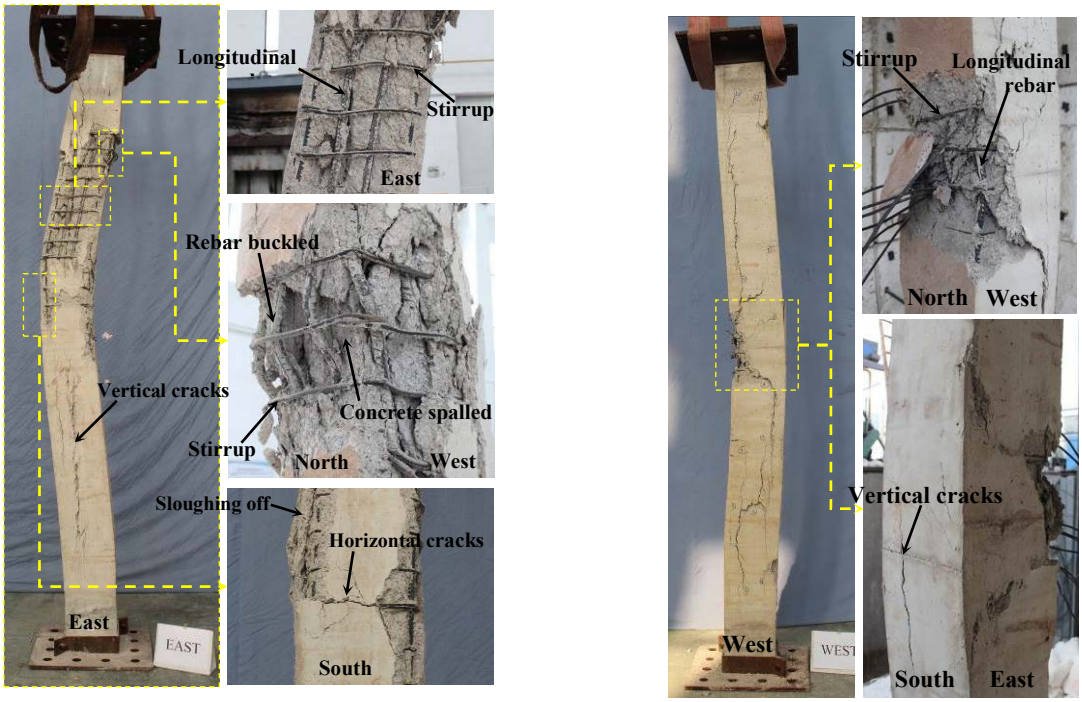

(a) Fire resistance test (b) Postfire test

Fig. 6. Failure modes of concrete-encased CFST column in fire tests.

Fig. 7 shows the measured furnace temperature (T) versus time (t) relationships of one postfire specimens. Some major findings include: (1) Plateau stage around 100°C of concrete near steel tube (points 2 and 3) are more obviously observed than the other parts. (2) Temperature differences are captured between the inner and outer tube surfaces. This may be related to 1) the possible movement of the measuring end and 2) the possible gap of the tube and concrete. (3) The inner cross-section attains its peak temperature much later than the outer in the postfire tests. (4) The temperature attained by inner CFST component is low due to the insulating effect provided by outer RC component. It indicated that the strength of the inner concrete was not dramatically reduced.

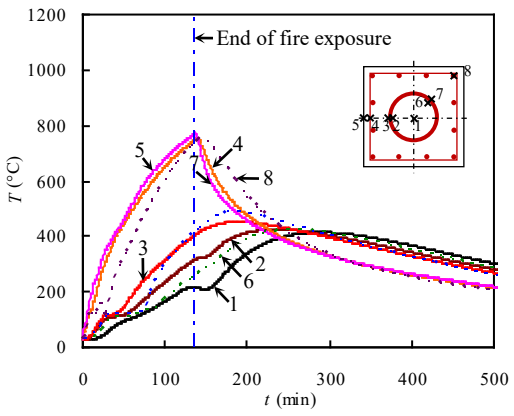

Fig. 7. Measured specimen temperature (T) versus time (t) relationships[21].

3. Construction considerations

3.1. Fabrication of the steel tube

For the straight seam welded steel tube and the spirally welded steel tube, the steel tube is made from the steel plate. For the seamless steel tube, the steel tube is made from a solid round steel billet. The manufacturing process of steel tubes differs with the manufacturing method. The assembly of joints should be conducted in professional steel factory. The inner surface of the steel tube shall be derusted before welding. The openings on the steel tube should be sealed before transport to keep the inside clean.

3.2. Casting of the concrete

Good performance shall be guaranteed for the inner concrete, such as high strength, high stiffness, low shrinkage, low creep, good workability, and no segregation or corrosion. For the concrete with strength greater than 60MPa, the mix proportion design should be trialled before construction. Before casting the concrete, a clean inner surface shall also be guaranteed.

The quality of concrete filling shall be checked after casting. One practical method is hitting the tube with a hammer from the outside. The defect in concrete would make different sounds at the tube over it. If any abnormity is detected, ultrasonic detection can be further used. The defects can be fixed by opening a hole on the tube, injecting high strength cement and closing the openings.

The outer RC component is constructed differently according to the construction methods. For the different-stage construction, the reinforcing cage is erected after the inner CFST component is finished. For the same-stage construction, the inner concrete and outer concrete are cast simultaneously after the reinforcing cage is erected. The reinforcing cage shall be derusted before placement. The self-consolidation concrete (SCC) and normal concrete are recommended for the RC component.

3.3. Construction of beam-column joints

The beam-column joint is crucial to the whole structural system. The concept of 'strong-joint and weak-member' shall be achieved in practical design. To ensure the continuity of the concrete-encased CFST columns, both the steel tube and the rebars in the column shall penetrate the joint area.

The concrete-encased CFST columns are usually connected to steel beam and RC beam. For the first kind of joint, the I-shaped steel beam can be connected to the steel tube by ring plates as shown in Fig. 8(a). The ring plates are prefabricated with the steel tube, and the steel beam can be connected in situ. For the second kind of joint, the longitudinal rebars in the RC beam are connected to the steel tube via ring plates or sleeves as shown in Fig. 8(b)(c). The ring plates and sleeves are also prefabricated. The ring plates can be connected to the rebars from both *x* and *y* directions shown in Fig. 8. The sleeve has advantage for the exterior joints and the staggered joints.

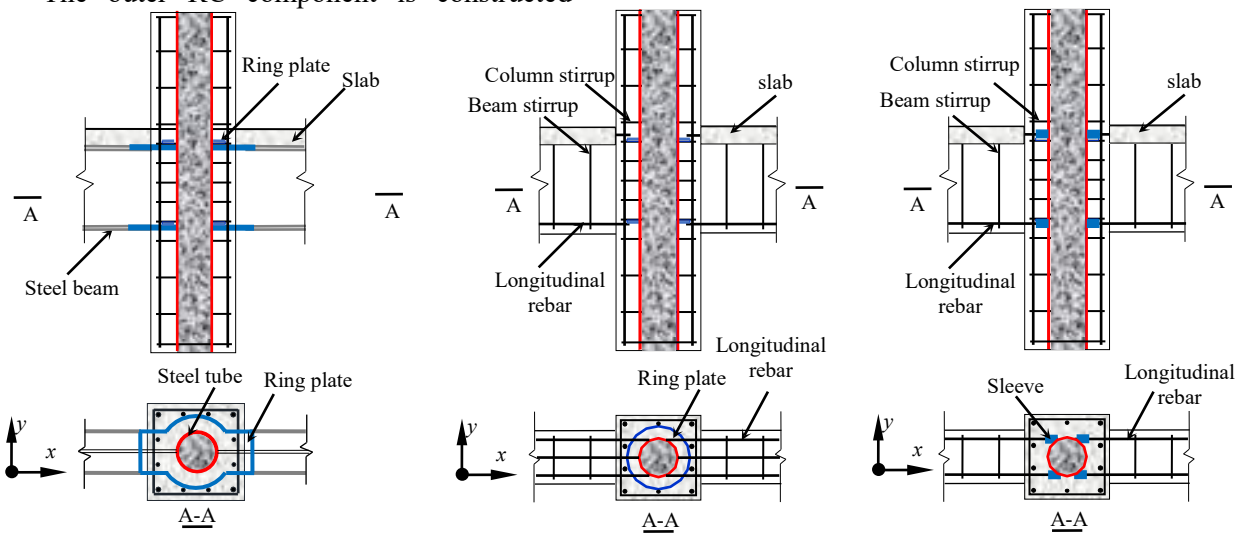

(a) Ring plate to steel beam joint (b) Ring plate to RC beam joint (c) Sleeve connection to RC beam joint

Fig. 8. The connection of concrete-encased CFST column joints.

To ensure a proper welding thickness, the thickness of the ring plate should be greater than the wall thickness of steel tube, the flange thickness of steel beam or the radius of rebars. For the sleeve connection, the anchorage length should be greater than the diameter of the rebar to ensure the enough anchorage force. To allow for proper casting room, the distance between adjacent sleeves should be greater than 25mm as well as the diameter of steel rebar.

4. Applications of concrete-encased CFST members

Concrete-encased CFST members have been used in China for more than two decades. They are gaining popularity in recent years in China due to the improvement of theory and technology. Concrete-encased CFST members have been used in buildings, bridges and other infrastructures in recent years. Some typical examples of these composite structures are presented below.

4.1. Buildings

The application history of concrete-encased CFST members in buildings can be divided into two stages: the initial stage and the later stage. In the initial stage (late 1990s), the concrete-encased CFST members are mainly used in the high-rise buildings in Shenyang due to the high requirement of earthquake resistance. In the later stage, the applications of concrete-encased CFST members spread to other cities of China.

Some examples of the initial stage are the Postal Terminal Building of Liaoning Province (96.6m in height, the first high-rise building using concrete-encased CFST columns in China, finished in 1996), Hetai Building, Local Taxation Bureau Building of Heping District, Electricity Garden, Fangyuan Building, Fulin Building, the Apartment of Liaoning Tourist Office and the Building of Liaoning Book's Publication. All these buildings are located in Shenyang, China.

From the twenty-first century, this kind of composite column has been accepted by more engineers. They were used in other provinces of China. Some examples include Zhuoyue-Huanggang Century Centre in Shenzhen, Huarun-Junyue Hotel in Shenzhen, Baoli Square in Shanghai, Tiancheng Building in Chongqing, Straits Exchange Centre Phase 2 in Xiamen and Changfu-Jinmao Tower in Shenzhen. Take Zhuoyue-Huanggang Century Centre as an example, the total height of the building is 280 m, and 22 concrete-encased CFST columns are used around the RC core tube. The dimension of the outer cross section and the diameter of the inner circular CFST are 1400 mm and 1060 mm, respectively. Concrete-encased CFST columns are also suitable in large-span buildings. It has been used as main supporting system in a large exhibition, the Urban and Rural Planning Exhibition of Guiyang in Guizhou Province.

4.2. Bridges

The applications of concrete-encased CFST members have also been extended to bridges in China since the twenty-first century. Concrete-encased CFST members have been used in arch bridge as arch ribs. Fig. 9(a) shows the Zhaohua Jialing River Bridge in Sichuan Province, China. The arch ring consists of two parallel arch ribs, and the arch length is 350 m. Six hollow steel tubes for each arch were established first. Then they were filled with concrete in order to resist the construction load. RC component was attached outside the CFST members to form the double-cell concrete-encased CFST box section.

In addition, concrete-encased CFST members have been used in rigid frame bridge as piers. Fig. 9(b) shows a photo of the Labajin Bridge on Longxi Express. One-cell concrete-encased CFST members with box section are used as piers in this bridge, whose highest pier is 182.5 meters. The steel tube is 1320 mm in diameter, and it is filled with high strength concrete. Fig. 10 presents two photos of the Heishigou Bridge during and after construction. This bridge is located in Sichuan Province and its piers are one-cell concrete-encased CFST with box sections.

(a) Zhaohua Jialing River Bridge (b) Labajin Bridge

Fig. 9. Concrete-encased CFST bridges [10].

(a) During construction (b) After construction

Fig. 10. Heishigou Bridge in Sichuan Province [10].

4.3. Other infrastructures

Concrete-encased CFST members have also been used in subway stations and workshops. Since the columns in subway stations are usually subjected to high axial compression and dynamic horizontal load, the concrete-encased CFST column is suitable to be served as supporting columns in these stations. For example, Laojie Station of Line 3 of Shenzhen Metro consists of four stories underground and sixteen floors above the ground. Concrete-encased CFST columns were adopted as the main supporting columns in the underground four stories.

In addition, concrete-encased CFST members have been used in industrial buildings in China. Fig. 11 shows two examples designed by the Huahui Design Group [19]. In these workshops, the concrete-encased CFST columns were easily connected to steel beams or RC beams.

(a) Concrete-encased CFST column to RC beam (b) Concrete-encased CFST column to steel beam

Fig. 11. Concrete-encased CFST in workshops [19].

5. Concluding remarks

The research and applications of concrete-encased CFST structures have developed rapidly over the past two decades. The scope of concrete-encased CFST structures has been extended greatly by researchers and engineers. This paper initially reviews the research on the structural performance of concrete-encased CFST members. Some design methods and construction considerations are introduced. Finally, the application history and typical projects using concrete-encased CFST columns are presented. Concrete-encased CFST structures can be used as an alternative to SRC and CFST systems. While the research on the structural behaviour of concrete-encased CFST structures is still at an early stage. Further researches on the performance of concrete-encased CFST column include creep and shrinkage behaviour, impact behaviour, fire performance, durability and construction issues. These future researches are essential to gain a better understanding of concrete-encased CFST structures and facilitate their applications.

Acknowledgments

The research reported in this paper is part of the Project 51678341 supported by the National Natural Science Foundation of China (NSFC). The financial support is highly appreciated.

References

[1]CEN. Design of composite steel and concrete structures, Eurocode 4, Brussels, Belgium; 2004.

[2]Han LH, Wang ZB, Xu W, Tao Z. Behavior of Concrete-Encased CFST Members under Axial Tension [J]. Journal of Structural Engineering 2016;142(2).

[3]Tao Z, Han LH, Uy B, Chen X. Post-fire bond between steel tube and concrete in concrete-filled steel tubular columns [J]. Journal of Constructional Steel Research 2011;67(3):360-378.

[4]Han LH, Li W, Tao Z, Wang WD. Advanced composite and mixed structures-Testing, theory and design approach (second version) [M]. Science Press, Beijing, China; 2016 [in Chinese].

[5]Han LH, An YF. Performance of concrete-encased CFST stub columns under axial compression. Journal of Constructional Steel Research 2014;93: 62-76.

[6]An YF, Han LH. Behaviour of concrete-encased CFST columns under combined compression and bending. Journal of Constructional Steel Research 2014;101:314-330.

[7]Li YJ, Han LH, Xu W, Tao Z. Circular concrete-encased concrete-filled steel tube (CFST) stub columns subjected to axial compression[J]. Magazine of Concrete Research 2016;68(19): 995-1010.

[8]Huang YS, Long YL, Cai J. Ultimate strength of rectangular concrete-filled steel tubular (CFT) stub columns under axial compression. Steel and Composite Structures 2008;8(2):115-128.

[9]An YF, Han LH, Roeder C. Flexural performance of concrete-encased concrete-filled steel tubes. Magazine of Concrete Research 2014;66(5):249-267.

[10]Han LH, An YF, Roeder C, Ren QX. Performance of concrete-encased CFST box members under bending. Journal of Constructional Steel Research 2015;106:138-153.

[11]Park HG, Lee HJ, Choi IR, Kim SB, Park SS. Concrete-filled steel tube columns encased with thin precast concrete. Journal of Structural Engineering 2015;141(12):04015056.

[12]Han LH, Liao FY, Tao Z, Hong Z. Performance of concrete filled steel tube reinforced concrete columns subjected to cyclic bending [J]. Journal of Constructional Steel Research 2009;65 (8-9): 1607-1616.

[13]Ji XD, Kang HZ, Chen XC, Qian JR. Seismic behavior and strength capacity of steel tube-reinforced concrete composite columns [J]. Earthquake Engineering and Structural Dynamics 2014;43(4):487-505.

[14]Wang ZB, Han LH, Li W, Tao Z. Seismic performance of concrete-encased CFST piers: experimental study[J]. Journal of Bridge Engineering 2016;21(4): 1084-0702.

[15]Shim CS., Chung YS, Han, JH. Cyclic response of concrete-encased composite columns with low steel ratio. Proceedings of the Institution of Civil Engineers-Structures and Buildings 2008;161(2):77-89.

[16]Qian WW, Li W, Han LH, Zhao XL. Analytical behavior of concrete-encased CFST columns under cyclic lateral loading. Journal of Constructional Steel Research 2016;120:206-220.

[17]Ma DY, Han LH, Li W, Zhao XL. Seismic Performance of Concrete-Encased CFST Piers: Analysis [J]. Journal of Bridge Engineering 2017;23(1):04017119.

[18]Ma DY, Li W, Han LH, Zhao XL. Finite element analysis on concrete-encased CFST column to reinforced concrete beam joints. 8th

conference on Steel and Aluminium structures, Honkong; 2016.

[19]Liao FY, Han LH, Tao Z. Behaviour of composite joints with concrete encased CFST columns under cyclic loading: Experiments[J]. Engineering Structures 2014;59:745-764.

[20]Han LH, Hu CM, Hou CC. Investigation on concrete-encased CFST members under laterally low velocity impact [J]. 13th International Conference on Steel Space and Composite Structures, Perth; 2018.

[21]Zhou K, Han LH. Experimental behavior of concrete-encased CFST columns after exposure to fire. 4th International Conference on Protective Structures (ICPS4), Beijing; 2016.

12th International Conference on Advances in Steel-Concrete Composite Structures (ASCCS 2018)
Universitat Politècnica de València, València, Spain, June 27-29, 2018
Doi: http://dx.doi.org/10.4995/ASCCS2018.2018.7205

Finite element analysis of concrete filled lean duplex stainless steel columns

D. Lam[a]*, J. Yang[a], and X.H. Dai[a]

[a]School of Engineering, Faculty of Engineering and Informatics, University of Bradford, UK
*corresponding author, e-mail address: d.lam1@bradford.ac.uk

Abstract

In recent years, a new low nickel content stainless steel (EN 1.4162) commonly referred as 'lean duplex stainless steel' has been developed, which has over two times the tensile strength of the more familiar austenitic stainless steel but at approximately half the cost. This paper presents the finite element analysis of concrete filled lean duplex stainless steel columns subjected to concentric axial compression. To predict the performance of this form of concrete filled composite columns, a finite element model was developed and finite element analyses were conducted. The finite element model was validated through comparisons of the results obtained from the experimental study. A parametric study was conducted to examine the effect of various parameters such as section size, wall thickness, infill concrete strength, etc. on the overall behaviour and compressive resistance of this form of composite columns. Through both experimental and numerical studies, the merits of using lean duplex stainless steel hollow sections in concrete filled composite columns are highlighted. In addition, a new formula based on the Eurocode 4 is proposed to predict the cross-section capacity of the concrete filled lean duplex stainless steel composite columns subjected to axial compression.

Keywords: *Lean duplex stainless steel; composite columns; axial compression; finite element model; cross-section capacity; Eurocode 4*

1. Introduction

Concrete filled steel tubes (CFSTs) have been used for high-rise buildings and bridges throughout the world. This increase is due to their advantages in constructability and superiority in strength. CFST columns consist of steel and concrete materials acting together contributed to the higher stiffness and load bearing capacity of these columns. [1]

Austenitic stainless steel is most widely used in the construction industry, however, a recently developed 'lean duplex' stainless steel which contains only 1.5% nickel offers a cheaper alternative. The particular grade used in this study is EN 1.4162, which is generally less expensive than the austenitic counterpart but offers higher strength, while maintaining a reasonable corrosion resistance. Numerous examples of lean duplex used in the construction could be found. Theofanous and Gardner [2] carried out experimental and numerical studies on the behaviour of lean duplex stainless steel square hollow sections (SHS) and rectangular hollow sections (RHS) subjected to axial compression, to investigate the effects of the sectional shape and wall thickness to the ultimate axial capacity. It was found that lean duplex sections offer superior strength when comparing to the austenitic counterparts, which in turn, provided a significant saving to the material cost.

Huang and Young [3] conducted finite element analysis (FEA) on cold-formed lean duplex stainless steel with square and rectangular hollow sections. An accurate finite element model has been created to simulate the pin-ended cold-formed lean duplex stainless steel short columns. The results showed that Eurocode 3 [4] and the Australian / New Zealand Standard [5] are relatively conservative in predicting the axial capacity of these form of hollow sections. Even though a significant number of researchers had conducted research

on the lean duplex stainless steel sections, there is little research had been carried out on CFST columns with lean duplex stainless steel tubes.

Lam and Giakoumelis [6] evaluated CFST columns under a variety of loading conditions with load applied: 1) on the steel and concrete simultaneously, 2) on the concrete alone and 3) on the concrete and steel with greased interface. The steel grades of S275 and S355 were used and the concrete strength varied from 30 to 100MPa. Results shown when the concrete and steel were loaded concurrently, the tube provided less confinement by comparison to the specimens that were only loaded to the concrete core, similar findings are also reported by Sakino *et al*. [7].

Studies on concrete filled carbon steel rectangular hollow section (RHS) composite columns have shown that width to thickness ratio of the steel elements and the constraining factor have significant influence to the compressive axial capacity and ductility of the concrete filled columns. [8-13] Research into CFST columns with high strength concrete infill has shown that high strength concrete infill provided enhancement in strength but led to reduction in ductility. [14-16] In terms of concrete filled composite columns with stainless steel sections, Uy *et al*. [17] tested 72 stub and 24 slender concrete filled stainless steel columns, with concrete strength varied between 20 to 75MPa, results on the stub column tests have shown that CFST with stainless steel tube has higher residual strength and ductile behaviour when compared to the carbon steel counterpart. An investigation into the behaviour of circular concrete filled lean duplex stainless steel tube using the finite element package ABAQUS [18] was reported by Hassanein et al. [19]. However, the FE model was validated using experimental studies on austenitic stainless steel columns carried out by Chang *et al*. [20] and the behaviour especially at the section capacity is quite different. It can be seen that previous research into lean duplex composite columns is relatively limited, little experimental study has been made on concrete filled composite columns with lean duplex stainless steel sections. [21] In the present study, a finite element model is developed and validated against the test results. Parametric studies were carried out over a range of concrete grades and steel thicknesses. The results of the parametric studies were used and compared with the existing design rule given in Eurocode 4 [22]. On the basis of the comparison, a new design expression based on the Eurocode 4 is proposed.

2. Finite element model

2.1. General

In this paper, finite element package ABAQUS 6.14 (RIKS method) is used to simulate the concrete filled lean duplex stainless steel stub column tests conducted by Lam *et al.* [21]. Geometry of the columns, materials, interactions, meshes, loading and boundary conditions of the FE model are defined accordingly and are described in the following sections.

The column specimens were subjected to concentric axial compression. Measured dimensions of the specimens are summarized in Table 1, where t_f, t_c denote the wall thickness at flat and corner portions of the stainless steel tube. Note that the tested concrete cube strength is 35.1 MPa, 61.2MPa and 81.0 MPa for the C30, C60 and C80 concrete specified in Table 1, respectively. SC1, SC2 and SC3 refer to square columns with steel tube dimensions of 60×60×3, 80×80×4 and 100×100×4 (unit: mm), respectively.

Table 1. Summarized measured stub column specimens dimensions in paper [21] (mm).

Column ID	$B \times H \times t_f \times t_c \times L$
SC1-C30	60.18×60.49×3.34×3.47×183.5
SC1-C60	59.96×60.34×3.41×3.68×184.5
SC1-C80	59.90×60.27×3.12×3.56×184.5
SC2-C30	80.27×80.16×3.82×4.19×243.5
SC2-C60	80.30×80.10×3.86×3.94×244.5
SC2-C80	80.19×80.42×3.73×4.05×244.5
SC3-C30	102.68×102.72×4.26×4.47×304.5
SC3-C60	102.93×102.52×3.99×4.42×304.5
SC3-C80	102.85×102.60×4.05×4.47×305.0

2.2. Steel material

The stress-strain model used for both the flat and corner regions of the lean duplex stainless steel tube in the FE model included of two parts. The first part is linear and up to the proportional limit stress with the measured elastic modulus E_0 (listed in Table 2 , Poisson's ratio 0.3). The second part is a converted true stress-strain curve based on tested data, e.g.

0.2% ($\sigma_{0.2}$), 1% proof stresses ($\sigma_{1.0}$), the ultimate stress (σ_u) and the strain at fracture (ε_f) by using Eqs. (1) and (2).

$$\sigma_{true} = \sigma_{nom}(1 + \varepsilon_{nom}) \quad (1)$$

$$\varepsilon_{ln}^{pl} = \ln(1 + \varepsilon_{nom}) - \frac{\sigma_{true}}{E} \quad (2)$$

where σ_{true} and σ_{nom} represent the true and engineering stress, respectively, and ε_{ln}^{pl} and ε_{nom} are the logarithmic plastic strain and engineering strain, respectively. The corner properties was extended to a distance of 2t beyond the curved portions of the stainless steel cross-sections, as suggested by Gardner and Nethercot [23].

Table 2. Measured steel material properties.

Section ID	E_0 (MPa)	$\sigma_{0.2}$	$\sigma_{1.0}$	σ_u	ε_f (%)
$S1_{flat}$	209800	755	819	839	44
$S1_{corner}$	212400	885	1024	1026	22
$S2_{flat}$	199900	679	736	773	42
$S2_{corner}$	210000	731	942	959	24
$S3_{flat}$	198800	586	632	761	47
$S3_{corner}$	206000	811	912	917	32

2.3. Concrete material

The Drucker–Prager model available in ABAQUS material library was adopted to simulate the behavior of concrete core.

A three-part constitutive model was used to define the material. The first part is assumed as an elastic part up to the proportional limit which is defined as $0.5f_c$ (concrete cylinder strength, assumed as 0.8 times of the cube strength). The initial modulus of elasticity E_c is calculated by the empirical equation ACI Committee 318 [24] as given in Eq. (3). Poisson's ratio of concrete is taken as 0.2. The corresponding strain (ε_c) is taken as 0.003 [23].

$$E_c = 4700\sqrt{f_c} \quad (3)$$

The second part starts from the proportional limit stress ($0.5f_c$) to the concrete strength (f_c). The equation proposed by Saenz [25] was adopted shown as follows (Eq. 4).

$$f = E_c\varepsilon/[1 + (R + R_E - 2)\left(\frac{\varepsilon}{\varepsilon_c}\right) - (2R - 1)\left(\frac{\varepsilon}{\varepsilon_c}\right)^2 + R\left(\frac{\varepsilon}{\varepsilon_c}\right)^3] \quad (4)$$

where $R_E = \frac{E_c\varepsilon_c}{f_c}$, $R = \frac{R_E(R_\sigma - 1)}{(R_\varepsilon - 1)^2} - \frac{1}{R_\varepsilon}$, $R_\sigma = R_\varepsilon = 4$ [26].

The third part is linear and starts from f_c to rkf_c while the corresponding strain is $11\varepsilon_c$. The value of r is taken as 1.0 and 0.5 for concrete with cube strength of 30MPa and 100MPa, respectively, while linear interpolation is used for cube strength between 30 and 100MPa [16]. The value of k can be calculated from a empirical equation given by Hu *et al*. [27] in Eq. (5).

$$k = 0.000178\left(\frac{B}{T}\right)^2 - 0.02492\left(\frac{B}{T}\right) + 1.2722 \quad \text{for } 17 \ll B/T \ll 70 \quad (5)$$

2.4. Meshes and interfaces

Three-dimensional 8-node solid elements (C3D8) were employed to discretize the concrete-filled square stainless steel stub column models. Generally, a mesh size equals to the tube wall thickness was adopted in the flat portions of the steel columns, while minimum of 3 elements along curvature was used at corners. For concrete core, a mesh size of two times of the wall thickness was used. Two layers of meshes were used in the tube wall thickness direction.

A surface-to-surface based interaction was adopted for the contact between steel tube (slave surface) and concrete core (master surface). In the direction tangential to the surface, the 'penalty' friction with a coefficient of friction equal to 0.3 was used, while 'hard contact' was used for the normal direction. End plates were included in the model to replicate the tests. The concrete was treated as slave surface in the interactions with the end plates.

2.5. Loading and boundary conditions

Load was applied axially through a reference point coupled to the top end plate by displacement control method. Both ends of the stub columns were restrained against all degrees of freedom, except for the displacement in the loading direction at the top. To reduce the calculation cost, a quarter model was simulated with symmetry boundaries in two directions.

3. Validation of the FE model

The FE model was validated with the load vs. displacement curves, ultimate capacities and failure modes of the concrete-filled lean duplex stainless steel columns tested. The comparison of the test and FEA curves is given in Fig. 1.

The column capacities recorded from tests and extracted from FEA is compared in Table 3. The average ratio of capacities N_{Test}/N_{FEA} is 0.98, with the standard deviation of 0.04 and the coefficient of variation (COV) of 0.044. The value of N_{Test}/N_{FEA} ranges from 0.88 to 1.02, within a satisfactory error of 12%. The failure modes observed from tests and predicted from FEA are shown in Fig. 2. It can be seen from the failure shapes and mode of failure (outwards local buckling), acceptable agreement was achieved. The developed FE model is deemed to be capable of predicting both the ultimate compressive strength and failure mode of the concrete-filled lean duplex stainless steel stub columns tested by Lam *et al*. [21].

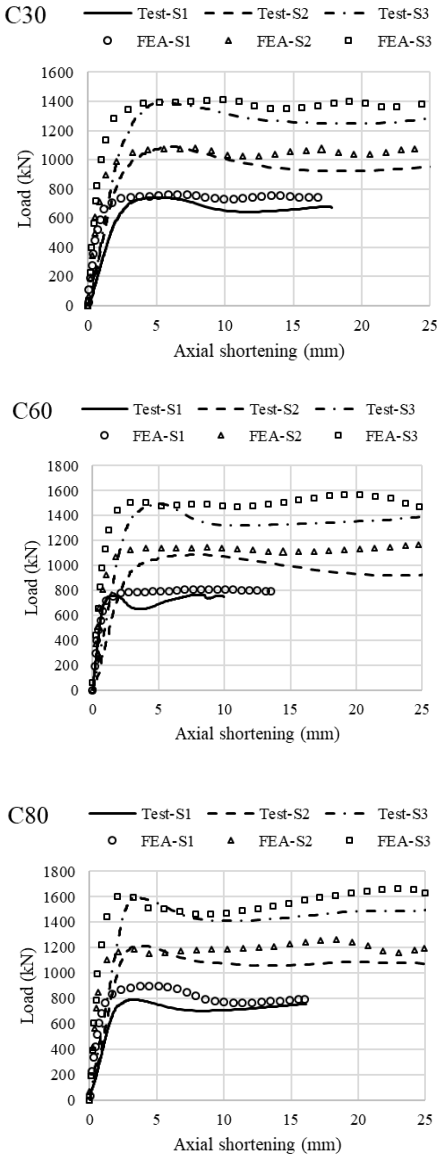

Fig. 1. Comparisons of load vs. displacement curves between test and FEA.

Table 3. Comparison of test and FEA results.

Column ID	N_{Test} (kN)	N_{FEA} (kN)	N_{Test}/N_{FEA}
SC1-C30	739	761	0.97
SC1-C60	759	808	0.94
SC1-C80	790	898	0.88
SC2-C30	1105	1079	1.02
SC2-C60	1160	1143	1.01
SC2-C80	1220	1193	1.02
SC3-C30	1394	1414	0.99
SC3-C60	1493	1519	0.98
SC3-C80	1599	1614	0.99
		Average	0.98
		Standard Deviation	0.04
		Coefficient of Variation	0.044

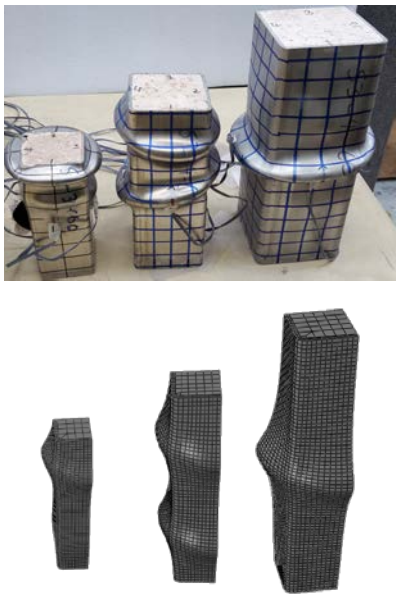

Fig. 2. Local buckling observed in both test and FEA results.

4. Parametric study

4.1. Parameters

A preliminary parametric study was carried out by using the validated FE model. A total of 24 stub column models were considered to assess the effect of concrete cylinder strength and steel tube cross-sectional geometry on the overall behaviour of the concrete-filled lean duplex stainless steel stub columns.

Table 4 summarizes the characteristics of the models. Overall 8 cross-sections were selected, ranging from 60×60×3 to 150×150×5, among which the ratio of outer width to tube wall thickness (B/t_f) varies from 20 to 40. The length of all the stub columns was equal to 3*B*.

Adopted concrete cylinder strength is 30MPa, 60MPa and 80MPa for each cross-section. In the parametric study, steel properties given in Table 2 for S1, S2 and S3 were used for cross-sections 60×60×3, 80×80×4 and 100×100×4, respectively. The properties of S1 were also used for cross-sections 100×100×3 and 120×120×3, and S3 for 120×120×4 and 150×150×5

Table 4. Details of concrete-filled lean duplex stainless steel stub columns considered in the parametric study.

Model ID	Concrete	B/t_f	N_{sc} (kN)
60×60×3	C30/60/80	20	682/748/784
80×80×4	C30/60/80	20	1114/1231/1299
100×100×3	C30/60/80	33.3	1217/1443/1601
100×100×4	C30/60/80	25	1306/1500/1634
100×100×5	C30/60/80	20	1593/1818/1970
120×120×3	C30/60/80	40	1472/1837/2087
120×120×4	C30/60/80	30	1606/1937/2170
150×150×5	C30/60/80	30	2510/3027/3390

4.2. Effect of concrete cylinder strength and section size

Fig. 3 shows the axial capacities of the columns increased with the increasing of concrete cylinder strength. The bigger the section size, the higher the increment. In other words, the capacity enhancement was more significant for the cross-section 120×120×3 than 60×60×3. This phenomenon resulted from the contributions of both the enlarged cross-sectional area of the tube and the amount of concrete infill.

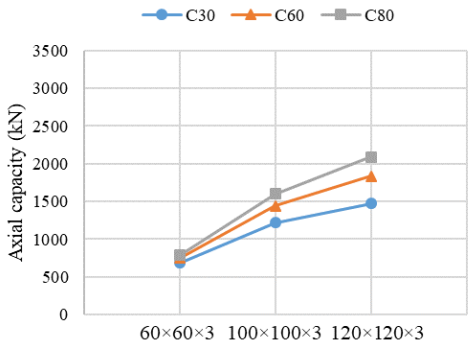

Fig. 3. Effect of cylinder strength and section size on axial compressive capacities of concrete-filled lean duplex stainless steel stub columns.

4.3. Effect of tube wall thickness

By maintaining the section size, the effect of tube wall thickness on the ultimate capacities of the columns was revealed, as shown in Fig. 4. The axial compressive capacity of the columns appeared to rise with the increasing of the tube wall thickness. The increase of the column capacity was more notable after the tube wall thickness was thicker than, i.e. 4mm in this case.

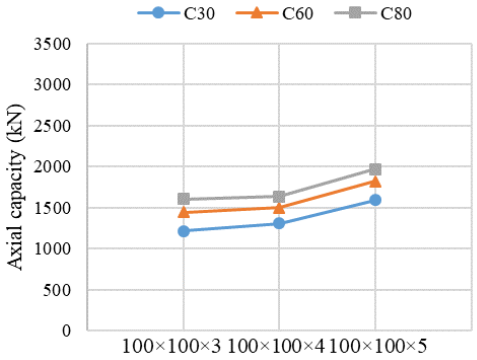

Fig. 4. Effect of tube wall thickness on axial compressive capacities of concrete-filled lean duplex stainless steel stub columns.

5. Prediction of axial compacity

The design equation, Eq. (6), provided in Eurocode 4 for concrete-filled carbon steel tube columns was firstly used to calculate the axial compressive capacities of the columns analyzed in the parametric study. The results showed that Eq. (6) for concrete filled carbon steel tube columns underestimated the axial capacity of the composite concrete filled columns with lean duplex stainless steel sections. Eq. (7) was then proposed for the prediction of the axial compressive capacity of concrete-filled lean duplex stainless steel columns. Eqs. (6)-(7) are given as follows,

$$N_{EC4} = A_s f_y + A_c f_{ck} \quad (6)$$

where

A_s is the cross section area of the steel section;

f_y is the yield stress of the steel section;

A_c is the cross section area of the concrete;

f_{ck} is the cylinder strength of the concrete.

$$N_{prop} = A_s \sigma_{1.0} + \varphi A_c f_{ck} \quad (7)$$

where

$\sigma_{1.0}$ is the steel strength at 1.0% strain;

φ is the confinement coefficient for the infilled concrete.

In this study, the confinement coefficient (φ) for the concrete infill is taken as 1.1 for simplicity. Table 5 shows the comparison of the parametric results vs. the new proposed design equation. The average ratio of capacities N_{para}/N_{prop} is 1.00, with the standard deviation of 0.05 and COV of 0.053. The average value of (for each cross-section with different concrete strengths) N_{sc}/N_{prop} ranges from 0.93 to 1.08, within a satisfactory average error of 8%.

Table 5. Comparison of parametric results vs. proposed design equation.

Model ID	N_{prop} (kN)	N_{sc}/N_{prop}
60×60×3	637/733/797	1.02
80×80×4	1035/1206/1320	1.03
100×100×3	1226/1517/1711	0.96
100×100×4	1224/1502/1688	1.01
100×100×5	1427/1693/1871	1.08
120×120×3	1559/1988/2274	0.93
120×120×4	1560/1974/2250	0.99
150×150×5	2438/3084/3515	0.99
	Average	1.00
	Standard Deviation	0.05
	Coefficient of Variation	0.053

6. Conclusions

Finite element analysis of concrete filled lean duplex stainless steel columns subjected to concentric axial compressive load was conducted in this paper. A finite element model was developed and validated through comparisons of the results obtained from the experimental study. A parametric study was then carried out to examine the effect of concrete cylinder strength, section size and tube wall thickness on the compressive capacity of the composite columns. Through both experimental and numerical studies, the merits of using lean duplex stainless steel hollow sections in concrete filled composite columns are highlighted. A new formula based on the Eurocode 4 is proposed to predict the cross-section capacity of the concrete filled lean duplex stainless steel composite columns subjected to axial compression. The results showed that the proposed equation could predict the axial capacity of concrete filled lean duplex stainless steel columns.

References

[1] Lam D, Gardner L. Structural design of stainless steel concrete filled columns. Journal of Constructional Steel Research 2008; 64(11):1275-1282.

[2] Theofanous M, Gardner L. Testing and numerical modelling of lean duplex stainless steel hollow section columns. Journal of Engineering Structures 2009; 31(12):3047-3058.

[3] Huang Y, Young B. Structural performance of cold-formed lean duplex stainless steel columns. Thin-Walled Structures 2014; 83: 59-69.

[4] CEN. Eurocode 3: EN1993-1-4 - Design of steel structures - Part 1.4: General rules - Supplementary rules for stainless steels. European Committee for Standardization; 2006.

[5] Australian / New Zealand Standard: AS/NZS 4673:2001. Cold-formed stainless steel structures. Standards Australia, Sydney, Australia; 2001.

[6] Giakoumelis G, Lam D. Axial capacity of circular concrete-filled tube columns. Journal of Constructional Steel Research 2004; 60(7):1049-1068.

[7] Sakino K, Tomii M, Watanabe K. Sustaining load capacity of plain concrete stub columns by circular steel tubes. In: Conference on concrete filled steel tubular construction 1998; 112-18.

[8] Uy B. Local and post-local buckling of concrete filled steel welded box columns. Journal of Constructional Steel Research 1998; 47(1-2):47-72.

[9] Uy B. Strength of short concrete filled high strength steel box columns. Journal of Constructional Steel Research 2001; 57(2):113-134.

[10] Han L, Yao G. Influence of concrete compaction on the strength of concrete-filled steel RHS columns. Journal of Constructional Steel Research 2003; 59(6):751-767.

[11] Mursi M, Uy B. Strength of concrete filled steel box columns incorporating interaction buckling. Journal of Structural Engineering 2003; 129(5):626-639.

[12] Lam D, Williams C. Experimental study on concrete filled square hollow sections. Steel and Composite Structures 2004; 4(2):95-112.

[13] Han L. Tests on stub columns of concrete-filled RHS sections. Journal of Constructional Steel Research 2002; 58(3):353-372.

[14] Rangan BV, Joyce M. Strength of eccentrically loaded slender steel tubular columns filled with high-strength concrete, ACI Structural Journal 1992; 89 (b):676-681.

[15] Kilpatrick AE, Rangan BV. Tests on high-strength composite concrete columns. Research Report No1/97, School of Civil Engineering, University of Technology, Western Australia; 1997.

[16] Ellobody E, Young B, Lam D. Behaviour of normal and high strength concrete-filled compact steel tube circular stub columns. Journal of Constructional Steel Research 2006; 62(7):706-715.

[17] Uy B, Tao Z, Han L. Behaviour of short and slender concrete-filled stainless steel tubular columns. Journal of Constructional Steel Research 2011; 67(3):360-378.

[18] ABAQUS. Analysis user's manuals and example problems manuals, version 6.9. Providence, Rhode Island: Abaqus Inc.; 2013.

[19] Hassanein M, Kharoob O, Liang Q. Behaviour of circular concrete-filled lean duplex stainless steel-carbon steel tubular short columns. Engineering Structures 2013; 56:83-94.

[20] Chang X, Ru ZL, Zhou W, Zhang Y-B. Study on concrete-filled stainless steel–carbon steel tubular (CFSCT) stub columns under compression. Thin-Walled Structures 2013; 63:125-33.

[21] Lam D Yang J, Mohammed A. Axial Behaviour of Concrete Filled Lean Duplex Stainless Steel Square Hollow Sections, Eurosteel 2017, Copenhagen, Denmark; 2017.

[22] CEN. EN 1994-1-1: Eurocode 4 - Design of composite steel and concrete structures. Part 1-1: General rules and rules for buildings. European Committee for Standardization; 2004.

[23] ACI 318-95. Building code requirements for structural concrete and commentary. Detroit (USA): American Concrete Institute; 1999.

[24] Saenz LP. Discussion of equation for the stress-strain curve of concrete. Journal of American Concrete Institute 1964; 61:1229-1235.

[25] Hu HT, Schnobrich WC. Constitutive modeling of concrete by using nonassociated plasticity. Journal of Materials in Civil Engineering 1989; 1(4):199-216.

[26] Hu HT, Huang CH, Wu MH, Wu YM. Nonlinear analysis of axially loaded concrete-filled tube columns with confinement effect. Journal of Structural Engineering, ASCE 2003; 129(10):1322-1329.

12th International Conference on Advances in Steel-Concrete Composite Structures (ASCCS 2018)
Universitat Politècnica de València, València, Spain, June 27-29, 2018
Doi: http://dx.doi.org/10.4995/ASCCS2018.2018.6949

Simplified numerical modelling of rectangular concrete-filled steel columns, beams and beam-columns

Z. Tao[a]*, U. Katwal[a], M. K. Hassan[a] and W. D. Wang[b]

[a]Centre for Infrastructure Engineering, Western Sydney University, Penrith, NSW 2751, Australia
[b]School of Civil Engineering, Lanzhou University of Technology, Lanzhou 730050, China
*corresponding author, e-mail address: z.tao@westernsydney.edu.au

Abstract

Because of its computational efficiency, simplified numerical modelling is the preferred method to simulate structural frames for routine design. As for concrete-filled steel tubular (CFST) columns, fibre beam element (FBE) modelling is often used in the simplified simulation. However, the accuracy of FBE modelling is greatly affected by the accuracy of the input material models, which should directly account for the interaction between the steel tube and core concrete. In this paper, simple yet accurate material models of steel and concrete are proposed for rectangular CFST columns by utilising a large amount of numerical data generated from detailed three-dimensional finite element modelling of stub columns. The material models are then incorporated into the simplified FBE simulation of rectangular CFST columns, beams and beam-columns. The accuracy of the simplified FBE simulation is verified by a wide range of experimental results on rectangular CFST stub columns, slender columns, beams and beam-columns.

Keywords: *Concrete-filled steel tubes; simplified simulation; confined concrete; local buckling; columns; beam-columns.*

1. Introduction

Concrete-filled steel tubular (CFST) columns have been widely used in modern construction because they offer many structural as well as economic benefits [1]. Although CFST columns with circular cross-section provide the strongest confinement to the core concrete, CFST columns with square or rectangular cross-sections are still increasingly used in construction due to the ease in the design of beam-to-column connections, high cross-sectional bending stiffness and the aesthetic considerations [1].

Because of its computational efficiency, simplified numerical modelling is the preferred method of simulating structural frames for routine design. Regarding CFST columns, fibre beam element (FBE) modelling is often used in the simplified simulation. However, the accuracy of such FBE modelling is greatly affected by the accuracy of the input material models, which should directly account for the interaction between the steel tube and core concrete, including the concrete confinement and buckling of the steel tube.

There are a few steel and concrete stress versus strain (σ–ε) models available in the literature developed for FBE modelling of square and rectangular CFST columns [2-5]. However, the majority of those material models are empirical and primarily derived from experimental data. They may give reasonable predictions within their validity ranges, but may not properly reflect the interaction between the steel tube and core concrete because the strength contributions from the steel and concrete core are not obtained explicitly. Meanwhile, the validity of an empirical model is restricted to the test data range used to derive the model parameters. Since there are increasing interests in using high-strength steel and concrete materials as well as thin-walled tubes, there is a strong need to develop simple yet accurate steel and

concrete models to cover a wide range of parameters for CFST columns.

To address the above research need, Katwal et al. [6] has recently proposed effective steel and concrete σ–ε models for circular CFST columns. This paper is a continuation of the previous work conducted by Katwal et al. [6]. The main aim of this study is to propose material models for rectangular CFST columns by utilising a large amount of numerical data generated from detailed three-dimensional (3D) finite element (FE) modelling of stub columns. The material models will then be incorporated into the simplified FBE simulation of rectangular CFST columns, beams and beam-columns. A wide range of experimental results on rectangular CFST stub columns, slender columns, beams and beam-columns will be utilised to verify the prediction accuracy of using the proposed material models.

2. Finite Element Modelling

The 3D FE model developed by Tao et al. [7] has been successfully used by Katwal et al. [6] to generate numerical data of circular CFST stub columns to cover a wide range of parameters. Based on regression analysis of these numerical data, Katwal et al. [6] developed effective σ–ε models for FBE modelling of circular CFST stub columns. The accuracy of the FBE modelling has been verified by comparing the numerical results with experimental results.

The above approach adopted by Katwal et al. [6] will also be used in this study to develop effective $\sigma - \varepsilon$ material models for square and rectangular CFST columns. The numerical simulations (including 3D FE and FBE analyses) were conducted using ABAQUS software. For the FBE modelling, the material models were implemented in ABAQUS through a UMAT subroutine. More details about the 3D FE modelling and FBE modelling of CFST columns can be found in Tao et al. [7] and Katwal et al. [6] respectively.

3. Development of Material Models For Fibre Beam Element Modelling

For a rectangular (square is a special case) CFST column under axial compression, interaction can be developed between the steel tube and concrete, resulting in the development of confinement to the concrete [7]. This confinement effect might lead to an increase in strength and ductility for the core concrete. However, this effect varies to a great extent depending on various column parameters, such as the cross-sectional dimensions of the steel tube (width B, height H and thickness t), steel yield stress (f_y) and unconfined concrete cylinder strength (f_c'). Meanwhile, tensile hoop stresses developed in the steel tube will reduce its load-carrying capacity in the axial direction [5]. Furthermore, local buckling of the rectangular steel tube can occur during the loading process, which also affects the interaction between the steel tube and concrete. The combined influence of all these factors is very complex and should be properly considered when proposing material models.

To develop effective steel and concrete $\sigma - \varepsilon$ models, 3D FE models were built for rectangular CFST stub columns covering a wide range of column parameters (f_y=186–960 MPa, f_c'=20–200 MPa and B/t=10–150). For each analysed example, the loads carried by the steel tube and core concrete were extracted from the middle section of the CFST column to generate "averaged" $\sigma - \varepsilon$ curves for the steel and concrete. Since the averaged $\sigma - \varepsilon$ curves have already incorporated the influence of interaction between the steel tube and concrete, they can be directly used in FBE modelling. Based on the numerical data, regression analysis is then conducted to propose effective steel and concrete models as described in the following subsections.

3.1. Steel Material Model

3.1.1 Characteristics of stress–strain curves for steel

In conducting 3D FE modelling of rectangular CFST stub columns, Tao et al. [7] adopted an elastic-perfectly plastic model for the steel. To reveal the influence of steel-concrete interaction on the effective $\sigma - \varepsilon$ curves of steel, typical columns with different confinement factors varied from 0.15 to 3.40 were analysed using the 3D FE modelling. The confinement factor defined in Tao et al.

[7] is expressed as $\xi_c=A_s f_y/A_c f_c'$, where A_s and A_c are the cross-sectional areas of the steel tube and concrete, respectively. The obtained effective axial $\sigma-\varepsilon$ curves of steel are compared in Fig. 1a for columns with different ξ_c-values. It can be clearly seen that the effective $\sigma-\varepsilon$ curves obtained from the 3D FE modelling are quite different from the input $\sigma-\varepsilon$ curve. This is due to the development of hoop stresses in the steel tube in combination with the influence of local buckling of the steel tube. The analysed examples highlight the need to develop an effective $\sigma-\varepsilon$ model of steel for the FBE modelling of rectangular CFST columns.

In general, the effective $\sigma-\varepsilon$ curves of steel in different columns follow a same linear relationship in the elastic stage. This is due to the weak interaction between the steel tube and core concrete in this stage [1]. But after reaching the peak stress, the effective $\sigma-\varepsilon$ curves enter into the post-peak stage. Depending on the ξ_c-value, the descending speeds of the curves are different. The smaller the ξ_c-value, the faster the curve descends. Similar observation has been reported by Katwal et al. [6] for circular CFST columns, which can be explained by the dilation effect of the concrete and the local buckling of the steel tube. For circular CFST columns, strain-hardening was observed beyond the critical point $(\varepsilon_{cr}', f_{cr}'/f_y)$ on the curve [6]. However, for rectangular CFST columns, no such strain-hardening can be found in the curves shown in Fig. 1a. This is due to the fact that steel tubes in rectangular CFST columns are more susceptible to local buckling compared to the steel tubes in the circular counterparts [1].

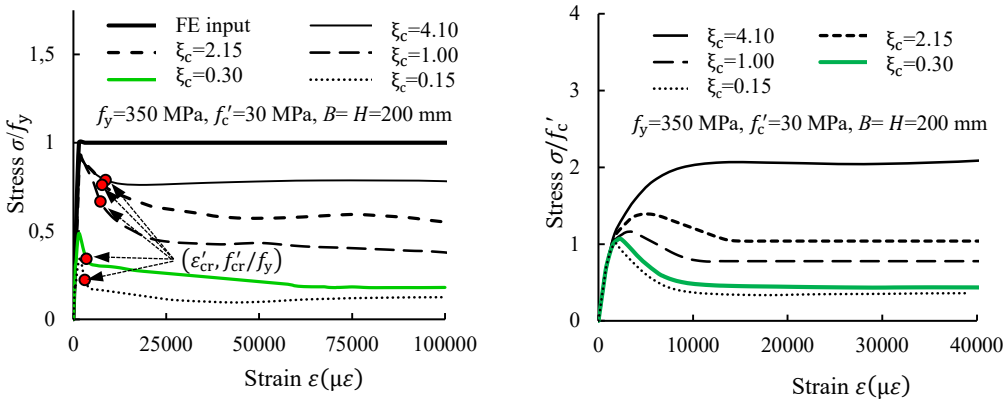

(a) Steel $\sigma-\varepsilon$ curves (b) Concrete $\sigma-\varepsilon$ curves

Fig. 1. Effective $\sigma-\varepsilon$ curves of steel and concrete.

3.1.2 Proposed steel stress–strain relationship

The effective $\sigma-\varepsilon$ model of steel expressed by Eq. (1) was originally proposed by Katwal et al. [6] for circular CFST columns.

$$\sigma=\begin{cases} E_s\varepsilon & 0\le\varepsilon<\varepsilon_y' \\ f_{cr}'-(f_{cr}'-f_y')\cdot\left(\frac{\varepsilon_{cr}'-\varepsilon}{\varepsilon_{cr}'-\varepsilon_y'}\right)^{\psi} & \varepsilon_y'\le\varepsilon<\varepsilon_{cr}' \\ f_u'-(f_u'-f_{cr}')\cdot\left(\frac{\varepsilon_u-\varepsilon}{\varepsilon_u-\varepsilon_{cr}'}\right)^{p} & \varepsilon_{cr}'\le\varepsilon<\varepsilon_u \\ f_u' & \varepsilon\ge\varepsilon_u \end{cases} \quad (1)$$

where E_s is the Young's modulus of steel; f_y' is the first peak stress of steel in the CFST column; ε_y' $(=f_y'/E_s)$ is the strain corresponding to f_y'; ψ and p are the strain softening exponents; ε_{cr}' and f_{cr}' are the critical strain and stress respectively; and f_u' is the effective stress of steel corresponding to the ultimate strain (ε_u). It is found that Eq. (1) can also be used for rectangular CFST columns if the parameters in the equation are recalibrated using the numerical data of rectangular CFST columns. Fig. 2 shows a schematic view of the simplified effective $\sigma-\varepsilon$ curves with low, medium and high ξ_c values for rectangular CFST columns. Six parameters $(f_y', f_{cr}', \varepsilon_{cr}', f_u', \psi,$ and $p)$ specifying the effective $\sigma-\varepsilon$ relationship need to be determined or recalibrated.

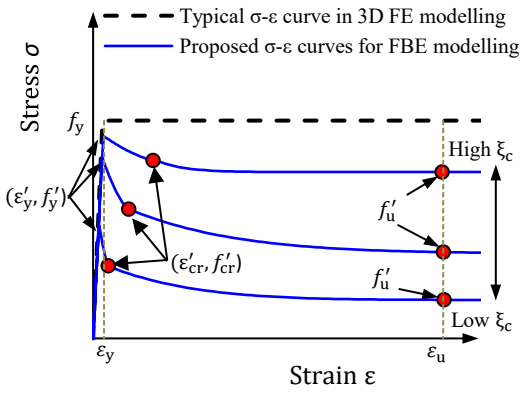

Fig. 2. Proposed steel σ–ε curves for FBE modelling of rectangular CFST columns.

It is found that f'_y can be calculated using Eq. (2) proposed by Wang et al. [8].

$$f'_y = f_y \cdot \left[0.91 + 7.31 \times 10^{-5} f_y - \left(1.28 \times 10^{-6} + 2.26 \times 10^{-8} f_y\right)\left(\frac{D'}{t}\right)^2\right] \quad (2)$$

where D' is the equivalent diameter defined as $\sqrt{B^2 + H^2}$. Eqs. (3)–(5) are proposed in this study to determine $f'_{cr}, \varepsilon'_{cr}$, and f'_u, respectively. These equations were derived based on regression analysis of the numerical data generated from 3D FE modelling.

$$f'_{cr} = f_y \cdot \left(2.15\xi_c^{0.02} - 0.002\frac{D'}{t} - 1.35\right) \quad (3)$$

$$\varepsilon'_{cr} = \varepsilon_y \cdot \left[6.5 - 0.035\frac{D'}{t}\left(1 - 0.0015\frac{D'}{t}\right) + 0.06\xi_c\right] \quad (4)$$

$$f'_u = f_y \cdot \left[1.2\xi_c^{0.02} - 0.2\left(\frac{D'}{t}\right)^{0.3}\right] \quad (5)$$

The value of ψ was suggested by Katwal et al. [6] as 1.5 for circular CFST columns. The same value is found to be applicable for rectangular CFST columns as well. Since the steel effective $\sigma - \varepsilon$ relationship for rectangular CFST columns does not have a strength recovery in the post-peak stage, the equation to determine p is recalibrated and given by Eq. (6).

$$p = -0.02E_s\left(\frac{\varepsilon_u - \varepsilon'_{cr}}{f'_u - f'_{cr}}\right) \quad (6)$$

3.2. Proposed Concrete Model

3.2.1 Characteristics of stress–strain curves for concrete

For the concrete infill in a CFST column, the compressive strength and ductility can be improved as a result of confinement. The confinement factor ξ_c can reasonably reflect the intensity of concrete confinement [1]. Effective concrete $\sigma - \varepsilon$ curves for rectangular CFST columns with different ξ_c-values are obtained from 3D FE modelling and compared in Fig. 1b. When the confinement is strong, an obvious increase in compressive strength and ductility can be obtained for the concrete. But when ξ_c is small, the increase in strength and ductility of the concrete is limited due to the relatively weak confinement. An effective concrete $\sigma - \varepsilon$ relationship is proposed in the following subsection to consider the confinement effect in rectangular CFST columns.

3.2.2 Proposed concrete stress–strain relationship

Eq. (7) was proposed by Katwal et al. [6] to represent the concrete stress–strain relationship for circular CFST columns. It is found that the same expression is also applicable for rectangular CFST columns.

$$\sigma = \begin{cases} \dfrac{A \cdot X + B \cdot X^2}{1 + (A-2) \cdot X + (B+1) \cdot X^2} \cdot f'_{cc} \\ X \le 1 \text{ or } (X > 1 \text{ and } \sigma > f_r) \\ f_r \qquad\qquad X > 1 \text{ and } \sigma \le f_r \end{cases} \quad (7)$$

$$X = \frac{\varepsilon}{\varepsilon'_{cc}} \quad (8)$$

where f'_{cc} and ε'_{cc} are the confined concrete strength and the corresponding ultimate strain; f_r is the residual stress of concrete; and A and B are the coefficients to determine the shape of the $\sigma - \varepsilon$ curve. Fig. 3 shows the schematic of $\sigma - \varepsilon$ curves with low and high ξ_c values. Five parameters (f'_{cc}, ε'_{cc}, f_r, A, and B) are required to define the full-range $\sigma - \varepsilon$ relationship of concrete.

To determine f'_{cc} and ε'_{cc}, the equations proposed by Wang et al. [8] are utilised in the present study which are represented by Eqs. (9) and (11), respectively.

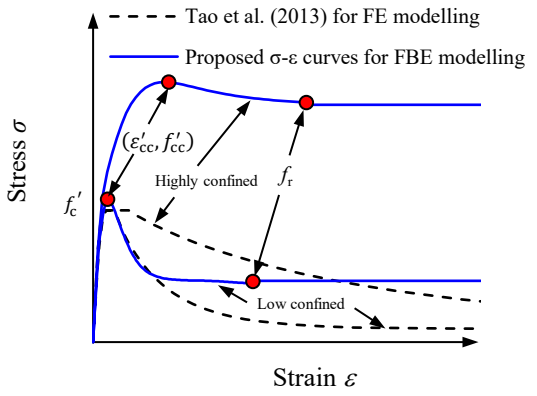

Fig. 3. Proposed concrete $\sigma-\varepsilon$ curves for FBE modelling of rectangular CFST columns.

$$f'_{cc} = f'_c\left[0.98 + \frac{29.5}{f_y^{0.48}} k_s{}^{0.2}\left(\frac{tf_y}{D'f'_c}\right)^{1.3}\right] \quad (9)$$

where k_s is the equivalent confining coefficient proposed by Lam and Teng [9]

$$k_s = \frac{1}{3}\left(\frac{B-2t}{H-2t}\right)^2 \quad (10)$$

$$\varepsilon'_{cc} = 2300 + 31.2f'_c + (2.32\times 10^4 - 3.88 \times 10^6 f_c'^{-1.8}\left(\frac{tf_y}{D'f'_c}\right)^2 \quad (11)$$

Based on regression analysis, Eq. (12) is proposed to determine f_r for rectangular CFST columns.

$$f_r = f'_{cc}\left(\sqrt{\frac{t}{D'f'_c}} + \frac{\sqrt{\xi_c}}{2}\right) \le f'_{cc} \quad (12)$$

Also based on regression analysis, Eqs. (13) and (14) are proposed to calculate A and B, respectively.

$$A = \alpha_1 \frac{E_c\varepsilon'_{cc}}{f'_{cc}} \quad (13)$$

where $\alpha_1 = 1 + 0.2\cdot\xi_c^{(0.05+0.2/\xi_c)}$; and E_c is the modulus of elasticity of concrete.

$$B = -0.005 - 0.7e^{(-0.3\xi_c^3)} \ge -0.75 \quad (14)$$

It should be noted that Eqs. (1) and (7) are only applicable for steel and concrete under compression. This paper intends to develop FBE models not only for stub columns under axial compression, but also for slender columns, beams and beam-columns, where part of the materials is likely subjected to tension. Therefore, the tensile material properties of steel and concrete need to be defined for simulation. For steel in tension, the $\sigma-\varepsilon$ relationship proposed by Tao et al. [10] is used in this study. As for concrete in tension, the tensile $\sigma-\varepsilon$ relationship proposed by Hassan [11] is used in the present study.

4. Validation of the Simplified Model

Test results of rectangular CFST stub columns, beams, slender columns, and beam-columns reported in the literature are used to verify the accuracy of the proposed material models for FBE modelling. Detailed comparisons between the predicted and measured results are given in the following subsections.

4.1. Stub Columns

The axial load−axial strain ($N-\varepsilon$) curves of 180 rectangular CFST stub columns collected from 21 sources were used to verify the proposed FBE model. Those test data were originally collected by Tao et al. [7] to develop 3D FE models, and the data cover a wide range of parameters: f_y =194–835 MPa; f'_c = 20–160 MPa; B = 60–500 mm; and D'/t =14–212.

Firstly, the predicted ultimate strengths (N_{uc}) are compared with the measured ultimate strengths (N_{ue}) in Fig. 4. Following the definition proposed by Tao et al. [7], the ultimate strength in this study is taken as the peak load if the $N-\varepsilon$ curve has a softening branch and the strain corresponding to the peak load is less than 0.01; otherwise the ultimate strength is defined as the load at 0.01. The mean (μ) and standard deviation (SD) of the N_{uc}/N_{ue} ratio are 0.951 and 0.073, respectively. This indicates a good correlation between the predicted and measured ultimate strengths. The predicted $N-\varepsilon$ curves are also compared with the measured curves of rectangular CFST stub columns. In general, the agreement between them is also very good. Due to the space limitation, only a few representative results are presented in this paper.

Katwal et al. [6] divided circular CFST columns into different groups based on the steel and concrete strengths. The concrete was classified into three categories: normal strength concrete (NSC: $f_c' \leq 60$ MPa), high strength concrete (HSC: 60 MPa $< f_c' \leq$ 120 MPa) and ultra-high strength concrete (UHSC: $f_c' > 120$ MPa). Similarly, the steel was classified into two categories: normal strength steel(NSS: $f_y \leq 460$ MPa) and high strength steel (HSS: $f_y > 460$ MPa). This classification method is also applied to rectangular CFST columns in this study.

Fig. 5 compares the predicted and measured $N-\varepsilon$ curves of a typical specimen 4HN with NSC and NSS, which was tested by Tomii et al. [12]. It can be seen that the predicted curve agrees very well with the measured curve and the curve predicted from the 3D FE modelling. The initial stiffness, ultimate strength, strength deterioration as well as the residual strength are well predicted by the FBE modelling. Based on the simulation, the loads carried by the steel tube and concrete are also presented in Fig. 5. Because the concrete has more contribution to the ultimate strength than the steel tube, this specimen has a high descending speed when entering into the post-peak stage.

To verify the prediction accuracy of the proposed FBE model for HSS tubes filled with HSC or UHSC, two specimens CR8-A-8 and S2 tested by Sakino et al. [2] and Xiong et al. [13], respectively, are selected for demonstration. The values of f_y for CR8-A-8 and S2 are 835 and 779 MPa and the corresponding values of f_c' are 74.8 and 152.4 MPa, respectively. The comparisons shown in Figs. 6 (specimen CR8-A-8) and 7 (specimen S2) indicate very good predictions by the FBE modeling.

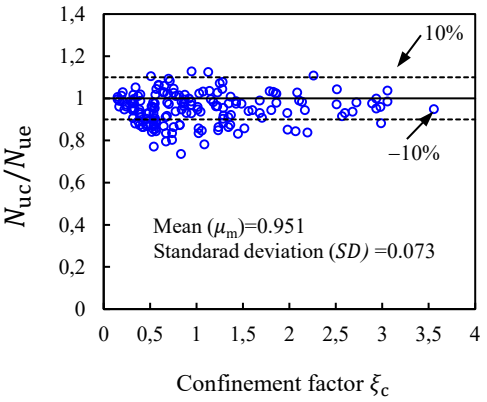

Fig. 4. Comparison between N_{uc}/N_{ue} with respect to ξ_c for CFST stub columns.

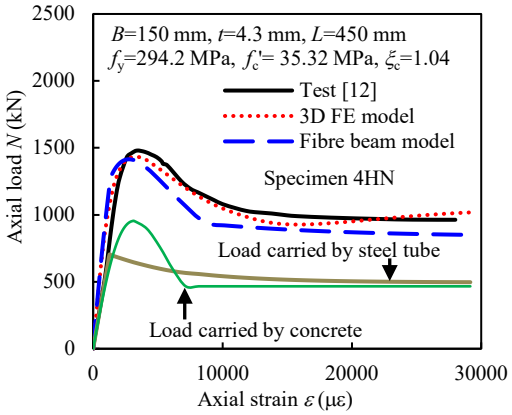

Fig. 5. Comparison of predicted and measured $N-\varepsilon$ curves for a typical specimen with NSC and NSS.

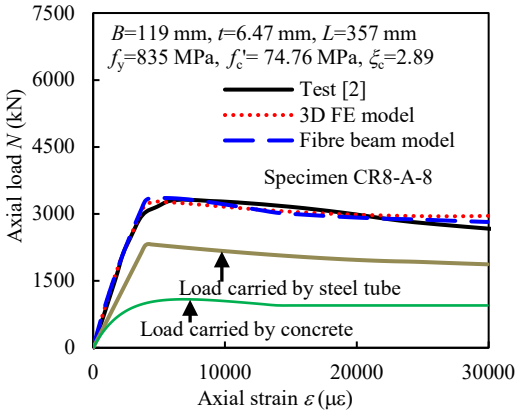

Fig. 6. Comparison of predicted and measured $N-\varepsilon$ curves for a typical specimen with HSC and HSS.

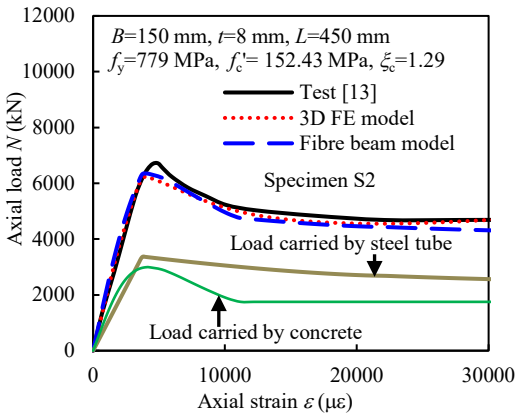

Fig. 7. Comparison of predicted and measured $N-\varepsilon$ curves for a typical specimen with UHSC and HSS.

4.2. Beams

Twelve CFST beams under pure bending tested by Gho and Liu [14] were selected to verify the proposed FBE model in simulating CFST beams. These specimens were simply-supported with one end hinged and the other end roller supported. Two point loads were applied at one-quarter of the span from each side. The span of the beams were 1460 mm. In general, reasonable prediction accuracy was obtained from the FBE modelling for all the twelve beams. The comparison between predicted and measured mid-span moment versus mid-span deflection (M–δ) for two typical specimens B02 and B10 are presented in Fig. 8. It can be seen that the predictions obtained from the FBE modelling are in good agreement with the test data.

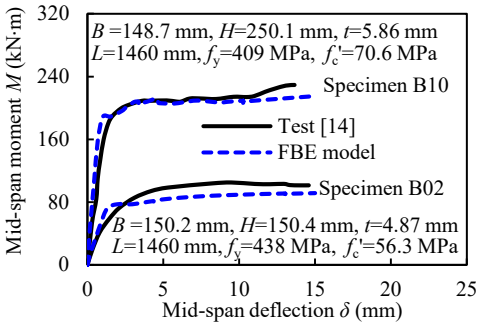

Fig. 8. Comparison of predicted and measured $M-\delta$ curves for a typical CFST beam.

4.3. Slender columns

Initial imperfections cause significant strength reduction for slender columns due to the second-order effect. Therefore, initial imperfections are included in this study to simulate slender CFST columns. This is achieved by scaling the first eigenvalue buckling mode shape. The amplitude of the imperfections is tentatively taken as $L/1000$ in the present study, where L is the length of the column. Further research can be conducted to determine more suitable values of the imperfection amplitude to improve the prediction accuracy.

Eight test data reported by Han et al. [15] are used in the present study to verify the proposed FBE model in simulating slender columns. In general, the axial load versus mid-span deflection (N–u_m) curves have been predicted reasonably well for all the selected slender columns. An example is presented in Fig. 9 for specimen scp2-1-1 with a slenderness ratio (λ) of 75. The ultimate strength of this specimen is underestimated by 8.8%, but the shape of the predicted curve agrees very well with that of the test curve.

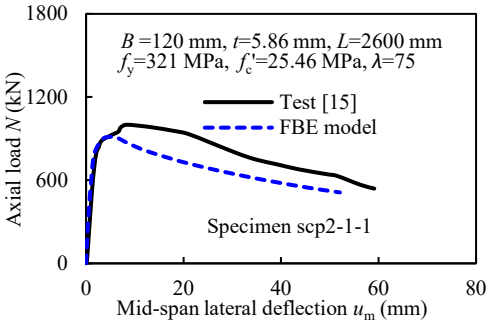

Fig. 9. Comparison of predicted and measured $N-u_m$ curves for a typical slender column.

4.4. Beam-columns

The FBE model is further verified by test data of beam-columns reported by Han et al. [15]. Initial imperfections are also considered in the FBE modelling. The N–u_m curves predicted from the FBE modelling and 3D FE modelling are compared in Fig. 10 with the measured curve of a typical beam-column specimen scp1-2-4. The predicted ultimate strength from the FBE modelling is 15.0% smaller than the measured strength and 5.9% smaller than the 3D FE prediction. It should be noted that the material models developed in Section 3 were based on CFST columns under concentric compression. The direct use of these models indicates the omission of any strain gradient effect, which may lead to the conservative prediction for scp1-2-4. Further

research is required to improve the prediction accuracy for beam-columns using FBE modelling.

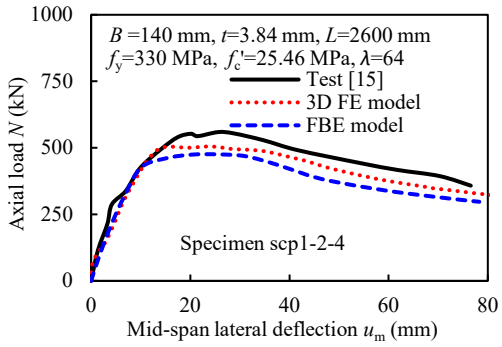

Fig. 10. Comparison of predicted and measured $N - u_{\mathrm{m}}$ curves for a typical beam-column.

Concluding remarks

In this paper, effective steel and concrete stress–strain models have been proposed for rectangular concrete-filled steel tubular columns based on detailed finite element modelling of stub columns under axial compression. The proposed stress–strain curves for steel have implicitly considered the interaction between the steel tube and concrete as well as local buckling of the steel tube. Meanwhile, the concrete model has considered the increase in strength and ductility resulting from the confinement.

The proposed material models were implemented in simplified fibre beam element modelling, and the predictions were verified by detailed FE modelling and a large amount of test data on rectangular CFST stub columns, beams, slender columns, and beam columns collected from the literature.

Further research can be conducted to account for the influence of global imperfections on slender columns and beam-columns and strain gradient effect. Moreover, this work can be extended to CFST columns with other cross-sectional shapes, e.g. polygonal, elliptical, etc. Because of the efficiency of FBE modelling, it is suitable to be used to analyse composite frames with CFST columns subjected to extreme events, such as fire, earthquakes, impact and blast. Further research is required in these areas.

References

[1] Han LH, Li W, Bjorhovde R. Developments and advanced applications of concrete-filled steel tubular (CFST) structures: Members. Journal of Constructional Steel Research 2014;100: 211-228.

[2] Sakino K, Nakahara H, Morino S, Nishiyama I. Behavior of centrally loaded concrete-filled steel-tube short columns. Journal of Structural Engineering, ASCE 2004;130: 180–188.

[3] Liang QQ, Uy B, Liew JYR. Nonlinear analysis of concrete-filled thin-walled steel box columns with local buckling effects. Journal of Constructional Steel Research 2006;62: 581-591.

[4] Thai HT, Uy B, Khan M. A modified stress-strain model accounting for the local buckling of thin-walled stub columns under axial compression. Journal of Constructional Steel Research 2015;111: 57-69.

[5] Lai Z, Varma AH. Effective stress-strain relationships for analysis of noncompact and slender filled composite (CFT) members. Engineering Structures 2016;124: 457-472.

[6] Katwal U, Tao Z, Hassan MK, Wang WD. Simplified numerical modelling of axially loaded circular concrete-filled steel stub columns. Journal of Structural Engineering, ASCE 2017;143(12): 04017169(1-12).

[7] Tao Z, Wang ZB, Yu Q. Finite element modelling of concrete-filled steel stub columns under axial compression. Journal of Constructional Steel Research 2013;89: 121-131.

[8] Wang ZB, Tao Z, Han LH, Uy B, Lam D, Kang WH. Strength, stiffness and ductility of concrete-filled steel columns under axial compression. Engineering Structures 2017;135: 209-221.

[9] Lam L, Teng JG. Design-oriented stress-strain model for FRP-confined concrete in rectangular columns. Journal of Reinforced plastic composites 2003;22(13): 1149-1186.

[10] Tao Z, Wang XQ, Uy B. Stress–strain curves of structural and reinforcing steels after exposure to elevated temperatures. Journal of Materials in Civil Engineering 2013;25(9): 1306–1316.

[11] Hassan MK. Behaviour of hybrid stainless-carbon steel composite beam-column joints. PhD thesis, Western Sydney University, Sydney, Australia; 2016.

[12] Tomii M, Yoshimura K, Morishita Y. Experimental studies on concrete filled steel tubular stub columns under concentric loading. Proceedings of the International Colloquium on Stability of Structures under

Static and Dynamic Loads. Washington DC, USA; 1977.

[13] Xiong MX, Xiong DX, Liew JYR. Axial performance of short concrete filled steel tubes with high- and ultra-high-strength materials. Engineering Structures 2017;136(4): 494–510.

[14] Gho WM, Liu D. Flexural behaviour of high-strength rectangular concrete-filled steel hollow sections. Journal of Constructional Steel Research 2004;60: 1681-1696.

[15] Han LH, Zhao XL, Tao Z. Tests and mechanics model for concrete-filled SHS stub columns, columns and beam-columns. Steel and Composite Structures 2001;1(1): 51-74.

12th International Conference on Advances in Steel-Concrete Composite Structures (ASCCS 2018)
Universitat Politècnica de València, València, Spain, June 27-29, 2018
Doi: http://dx.doi.org/10.4995/ASCCS2018.2018.7140

Behaviour of steel and composite beam-column joints subjected to quasi-static and impact loads

K. Chen[a], K. H. Tan[a]*

[a]Nanyang Technological University, Singapore
*corresponding author, e-mail address: ckhtan@ntu.edu.sg

Abstract

The behaviour of steel and composite beam-column joints was investigated in this paper. A test programme on typical beam-column joints subjected to quasi-static and impact loads was presented. A comparison of different connections was conducted and composite slab effect was investigated. Based on the test results, a component-based modelling approach was proposed and validated. Basic nonlinear springs of beam-column joint models were developed. Mechanical properties of the nonlinear springs were defined based on either current design codes or models proposed by previous researchers. Good agreement with test results was achieved by the component-based models.

Keywords: *Beam-column joint; impact load; column removal; progressive collpase*

1. Introduction

Beam-column joints play an import role in the robustness of building structures when structures are subjected to progressive collapse scenarios. Currently, many tests have been conducted on both fin plate (FP) [1-5] and welded unreinforced flange with bolted web (WUF-B) [6-12] connections. However, most of the previous tests focused on the behaviour of bare steel joints. The potential benefit of composite slab has not been fully investigated so far. Moreover, progressive collapse is a dynamic process in nature. Therefore, it is urgent to study the dynamic behaviour of beam-column joints. To meet the technical gaps, a test programme and a component-based modelling approach for beam-column joints subjected to quasi-static and impact loads are presented in this paper.

2. Experimental study

2.1. Test programme

A total of twelve half-scale beam-column joints with FP and WUF-B connections were designed based on Eurocode 3 Part 1-1, Eurocode 4 Part 1-1 [13, 14], AISC 360 [15] and AISC 325 [16] and their detailed information is provided in Table 1. Recommendations in FEMA 350 [17] were also considered. To identify each specimen, they are named based on the concrete slab thickness and connection detailing, such as C75 stands for 75 mm thick composite slab, FP for fin plate connection, W for WUF-B connection, M for the middle joint while S for the side joint, R for reduced number of shear studs, slot for slotted holes and rbs for reduced beam section. For instance, specimen C75FP-Mslot was a middle joint with 75 mm thick composite slab, fin plate connection and slotted bolt holes were used in the fin plates. For all the specimens, Grade S355 universal beams (UB 203×133×30) and columns (UC 203×133×71) were used and connected by Grade S275 fin plates and Grade 10.9 M20 bolts. A pre-torque of 280 kNm was applied to the bolts.

Eleven half-scale beam-column joints with FP and WUF-B connections were tested under impact loads and the details are shown in Table 2. The nomenclature is as follows: C stands for composite slab, FP for fin plate, W for WUF-B, M for mass, and H for height. For instance, specimen C75FP-M530H3 had a 75 mm thick composite slab and fin plate connections. It was subjected to an impact load from a 530 kg mass hammer dropping from 3 m height.

Table 1. Summary of quasi-static test specimens.

ID	Slab (mm)	Joint location	Shear studs
FP-static	/	/	/
C75FP-M	75	Middle	2 rows @ 90 mm
C75FP-S	75	Side	2 rows @ 90 mm
C100FP-M	100	Middle	2 rows @ 90 mm
C75FP-MR	75	Middle	1 row @ 180 mm
C75FP-Mslot	75	Middle	2 rows @ 90 mm
W-static	/	/	/
C75W-M	75	Middle	2 rows @ 90 mm
C75W-S	75	Side	2 rows @ 90 mm
C100W-M	100	Middle	2 rows @ 90 mm
C75W-MR	75	Middle	1 row @ 180 mm
C75W-Mrbs	75	Middle	2 rows @ 90 mm

Nomenclature: C - Composite; FP - Fin plate; W - WUF-B; M - Middle joint; S - Side joint; R - Reduced number of shear studs; slot - slotted holes; rbs - reduced beam section

Table 2. Summary of impact test specimens.

ID	Drop-weight (kg)	Height (m)	Impact velocity (m/s)
FP6-M530H3	530	3.015	7.389
FP10-M530H3	530	3.015	7.305
C75FP-M530H3	530	3	7.518
C75FP-M770H1.425	770	1.425	5.020
C75FP-M530H3-S	530	2.994	7.388
C100FP-M530H3	530	2.995	7.469
W-M830H3	830	2.993	7.235
C75W-M770H3	770	2.998	7.619
C75W-M770H2	770	2.005	6.230
C75W-M770H3-S	770	2.997	7.357
C100W-M770H3	770	2.996	7.357

Nomenclature: C - Composite; FP - Fin plate; M - Mass, kg; H - Drop-height, m; S - Side joint

Based on standard 150 mm diameter by 300 mm length cylinder tests, concrete compressive strength and the corresponding standard derivation are shown in Table 3.

Table 3. Concrete material properties.

Test series	Compressive strength (MPa)	Standard derivation (MPa)
FP quasi-static	36.7	2.8
WUF-B quasi-static	37.4	1.4
FP impact	37.0	3.6
WUF-B impact	50.6	5.4

A hydraulic actuator with displacement control at 6 mm/min was employed to apply a quasi-static load to beam-column specimens as shown in Fig. 1. The actuator has a capacity of 500 kN. The quasi-static load was monotonically applied on the middle column joint for a vertical 'push-down' test to find the maximum capacity. On the left side, a strong A-frame was used to simulate a pinned support while on the right side the specimens were connected to a pinned support reacting against a strong wall. The two pinned supports were used to simulate the inflexion points located roughly at the one-third span of each beam after the middle column was removed. The beam span was 3668 mm, smaller than a typical full-scale steel frame, to fit within the limited space in the laboratory. The test set-up was validated by tests conducted previously by Yang and Tan [18].

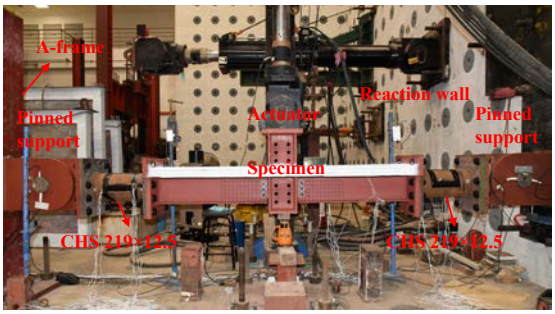

Fig. 1. Front view of quasi-static test set-up.

Fig. 2 shows the impact test set-up. An MTS drop-weight test machine was used to apply impact loads in the test programme. The basic drop-weight of the hammer system was 530 kg including a load cell system (60 kg). The drop-weight could be increased to 830 kg by adding 10 pieces of steel plates each weighing 30 kg. The impact hammer was centred to the axis of the middle column joint.

Fig. 2. Front view of impact test set-up.

2.2. Test results

Fig. 3 shows the development of static load versus displacement of four typical middle beam-column joints subjected to quasi-static loads. Bare steel joint FP-static was unable to sustain applied load at the initial stage (Fig. 3(a)) due to free rotation of its pin connection. The peak load was obtained at 82.9 mm and after that, fracture of fin plates occurred so that the applied load decreased dramatically. In contrast, C75FP-M was able to sustain 45 kN of applied load at the initial stage until crushing of concrete occurred due to the composite slab effect (Fig. 3(b)). However, due to greater demand on deformation capacity of the fin plates at the initial stage, fracture of the fin plate in C75FP-M occurred at a smaller displacement than FP-static (42 mm versus 82.9 mm). Since W-static had a stronger beam-column connection compared to FP-static, a greater load (Fig. 3(c)) could be resisted. W-static was more ductile when comparing final displacement at failure (400 mm versus 300 mm for FP-static). Due to the composite slab effect, a greater load could be resisted by C75W-M (Fig. 3(d)) at the initial stage. However, due to greater demand on deformation capacity of beam flanges, both the bottom and top beam flanges fractured at a smaller displacement compared with W-static.

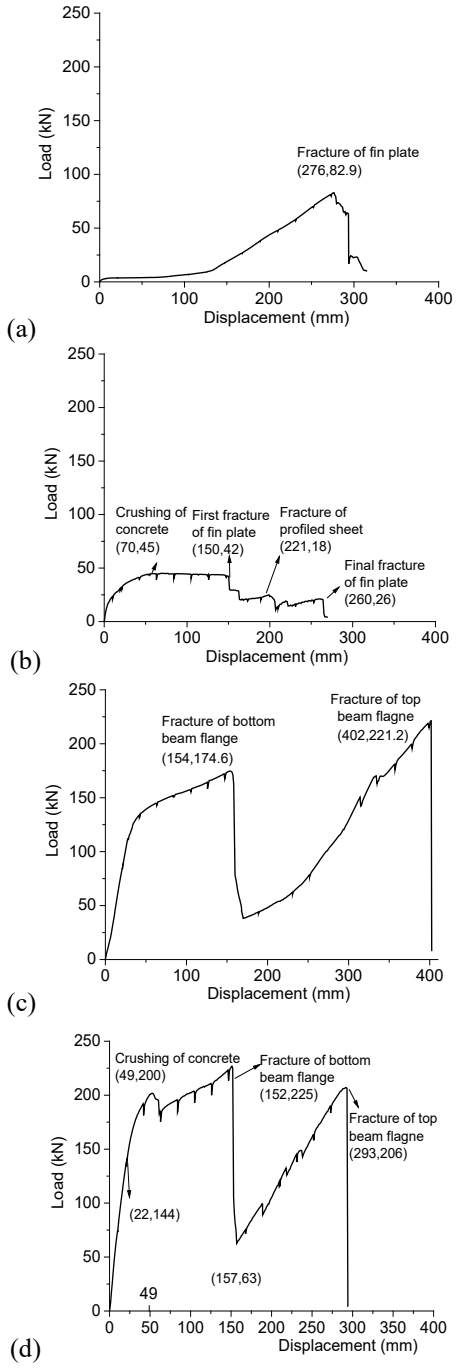

Fig. 3. Load versus displacement curves of typical quasi-static test specimens: (a) FP-static; (b) C75FP-M; (c) W-static; (d) C75FP-M

Fig. 4 shows the structural response of four typical beam-column joints subjected to impact loads. Specimen FP6-M530H3 had a 6 mm thick fin plate (bare steel connection) and the impact force development is shown in Fig. 4(a). Each collision consisting of three spikes in Fig. 4(a) represented one visible impact between the hammer head and the specimen. The first spike occurred when the hammer came in contact with the joint. Then the joint rebounded quickly due to horizontal restraint provided by the pinned

supports. In the test conducted by Grimsmo el al. [19], horizontal restraint was not applied so that only one spike was observed for each collision. C75FP-M530H3 was a composite FP joint and had a greater inertia compared to FP6-M530H3. Therefore, a greater peak impact force was observed (1067.8 kN versus 912 kN for FP6-M530H3) as shown in Fig. 4(b) while the velocity in terms of the slope of displacement versus time curve (Fig. 4(c)) was smaller. Specimen W-M830H3 had a welded connection to the column flange and thus it was much stiffer and stronger than fin plate specimen FP6-M530H3. A greater drop-weight of 830 kg was employed compared to FP6-M530H3. Therefore, a greater peak impact load (999.1 kN) was observed as shown in Fig. 4 (d). A stable period was observed between 15 ms and 50 ms for W-M830H3, which was also found in the impact test conducted by Fujikake el al. [20]. A similar phenomenon was observed for C75W-M770H3. Due to greater inertia compared to the bare steel joint, C75W-M770H3 had a greater peak impact force (1188.9 kN versus 999.1 kN for W-M830H3) as shown in Fig. 4(e). Complete fracture of the connection was not observed in the WUF-B joints. The respective residual displacements caused by plastic deformation were 112.8 mm for W-M830H3 and 50.3 mm for C75W-M770H3 (Fig. 4(f)).

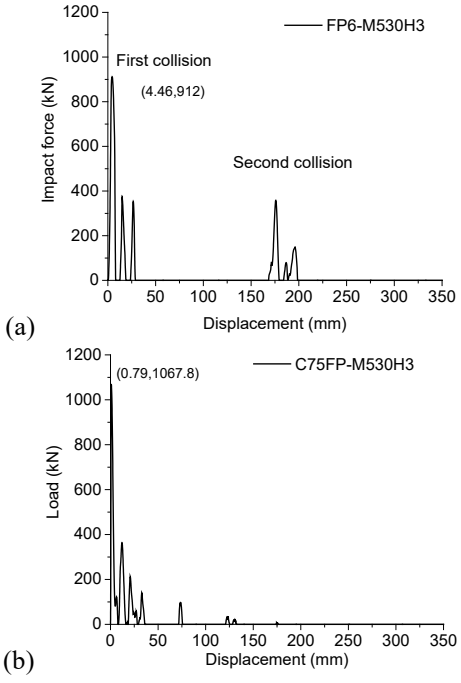

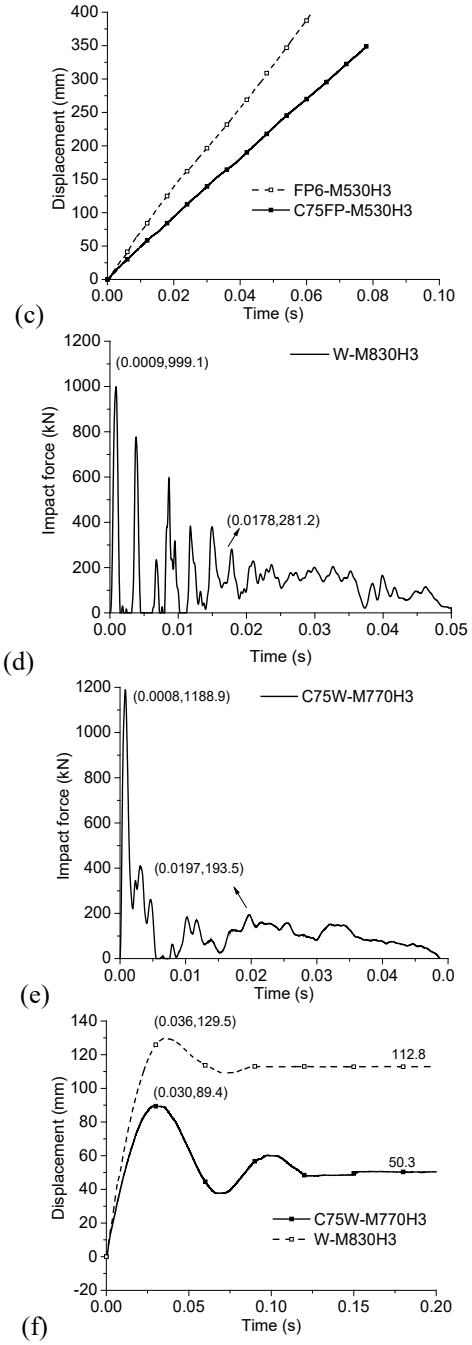

Fig. 4. Structural responses of typical impact test specimens: (a) Impact force development of FP6-M530H3; (b) Impact force development of C75FP-M530H3; (c) Displacement development of FP specimens; (d) Impact force development of W-M830H3; (e) Impact force development of C75W-M770H3; (f) Displacement development of WUF-B specimens.

3. Numerical study

Component-based models have been proposed for bolted angle and end plate connections subjected to column removal scenarios [21, 22]. In this paper, they are used to simulate beam-column joints with FP and WUF-

B connections. Nonlinear springs in the component-based models include the concrete slab, reinforcing bar, profiled sheeting, steel beam flange and bolted connection.

3.1 Concrete slab

Concrete properties can be obtained from either codified models or concrete material tests. For instance, concrete stress-strain relationship in uniaxial compression and tension can be adopted from the *fib* Model Code [23]. In this work, the contribution of concrete tension force is neglected.

In the experimental tests, failure of concrete was observed in a region at a distance roughly equal to one beam depth (h_b) from the column flange. Therefore, gauge length (h_g) of the concrete spring is set as the beam depth plus half the column depth, which is calculated from the column centreline. The peak compression force (F_{cm}) of concrete spring is equal to the tension force provided by the steel components including the beam flange, bolt rows, and profiled sheeting. Therefore, for each connection type, individual concrete spring property must be defined. It should be noted that F_{cm} should not exceed the maximum compressive resistance of the concrete slab, equal to the area of concrete (A_c) multiply by cylinder compressive strength (f_{cm}).

3.2. Reinforcing bar

Under compression, crushing and spalling of concrete surface can accelerate buckling of reinforcing bars, which was observed in the test. Therefore, compressive strength of reinforcing bars may be negligible. A bilinear curve of a tensile spring representing the reinforcing bars based on the yield strength σ_y , ultimate strength σ_u, elastic modulus E and nominal area of the bars is used. Only continuous reinforcing bars are considered while discontinuous bars are ignored. Gauge length (h_g) of the reinforcing bar spring is the same as that of the concrete spring.

3.3. Profiled sheeting

Since the thickness of the steel profiled sheeting is 1 mm, local buckling can substantially weaken its compressive resistance. Therefore, profiled sheeting in compression is negligible. Profiled sheeting in tension is simplified as a bilinear curve [21] based on coupon tests.

3.4. Beam flange

For fin plate connections, gaps exist between the beam flange and the column flange. The stiffness and resistance of the beam flange and the column flange in compression are much greater than those of a bolt row. Therefore, it is assumed that the stiffness and resistance of the beam flange and the column flange are infinite when the gap between them closes up.

For WUF-B connections, top and bottom beam flanges are welded to the column flange. Beam flange spring can be simplified as a simply-supported column element with a gauge length equal to one beam depth. The column element has the same rectangular cross-section as the beam flange.

3.5. Bolted connection

The behaviour of bolted connections in both compression and tension has to be considered.

a) Bolts in bearing between fin plate and beam web

Several methods have been proposed to predict the ultimate strength $R_{n,br}$ of bolts in bearing and they are included in national design codes such as Eurocode 3 Part 1-8 [13], AISC 360-10 [15] and CSA S16-09 [24]. The equation in Eurocode 3 Part 1-8 [13] gave a more conservative strength prediction compared to the AISC and CSA codes. Therefore, for more accurate predictions of the joint behaviour, the equation in AISC 360-10 is adopted as follows:

$$R_{n,br} = 1.5(L_e - \frac{d_b}{2})t\sigma_u \leq 3td_b\sigma_u \quad (1)$$

where L_e is the end distance from the centre of a bolt hole to the edge of the fin plate measured in the direction of load transfer (horizontal direction), d_b is the nominal diameter of the bolt, t is the thickness of the plate, and σ_u is the ultimate strength of the steel plate.

Fin plates may fail in block tearing mode prior to bolt bearing failure when the end distance is not adequate [25]. In this instance, bolt in bearing resistance in Eq. (1) cannot be achieved and block tearing resistance is used instead. Eurocode 3 Part 1-8 [13] provides block tearing resistance as follows:

$$R_{n,bs} = \sigma_u A_{nt} + (1/\sqrt{3})\sigma_y A_{nv} \quad (2)$$

where A_{nt} is net area subjected to tension and A_{nv} is net area subjected to shear.

The stiffness of bolt in bearing k_i is determined from Eq. (3) proposed by Rex and Easterling [26]:

$$k_i = \frac{1}{\frac{1}{k_{br}}+\frac{1}{k_b}+\frac{1}{k_v}} \quad (3)$$

where k_{br}, k_b and k_v are the stiffness values of bolt bearing, edge steel plate bending and shearing, respectively. They are specified by Eqs. (4) to (6).

$$k_{br} = 120t\sigma_y d_b^{(4/5)} \quad (4)$$

$$k_b = 32Et(\frac{L_e}{d_b} - \frac{1}{2})^3 \quad (5)$$

$$k_v = (20/3)Gt(\frac{L_e}{d_b} - \frac{1}{2}) \quad (6)$$

where σ_y is the yield strength, E and G are the respective moduli of elasticity and shear of the steel plate.

Rex and Easterling [27] proposed force-displacement relationship of bolts in bearing based on experimental tests. The relationship is capable of predicting the behaviour of steel joints with reasonable accuracy [28-31]. Therefore, the method is used to represent the constitutive relationship for bolts in bearing, as expressed in Eq. (7).

$$F_{br} = R_{n.br}[\frac{1.74\bar{\Delta}}{(1+\bar{\Delta}^{0.5})^2} - 0.009\bar{\Delta}] \quad (7)$$

where F_{br} is the resultant force, $\bar{\Delta} = \frac{\Delta k_i}{R_{n,br}}$ is the normalised displacement, and Δ is the displacement.

The main difference between the bolt rows in compression and tension arises from the bearing resistance at the bolt holes. In compression, the resistance of bolts in bearing can be calculated from Eq. (8).

$$R_{n,br} = 3td_b\sigma_u \quad (8)$$

The stiffness of bolt rows in compression can be determined by Eq. (3).

b) Bolts in shear

When shear failure of bolt shank governs failure mode of bolted connections, properties of bolts in shear should be used.

The ultimate strength of bolts in single shear is determined by Eq. (9).

$$R_{nv,bolt} = 0.6\frac{\pi d_b^2}{4}\sigma_{ub} \quad (9)$$

where σ_{ub} is the ultimate strength of the bolt.

c) Influence of oversized bolt hole and friction

Typically, an oversized bolt hole is used in construction practice to facilitate the installation of bolts. It can be predicted that the bolt shank moves towards the gap before contacting the steel plate, as shown in Fig. 5. Movement of the bolt shank may vary from 0 to twice the gap distance. In simulations, it can be assumed that the axis of bolt shank is concentric with the centroid of plate holes for simplification.

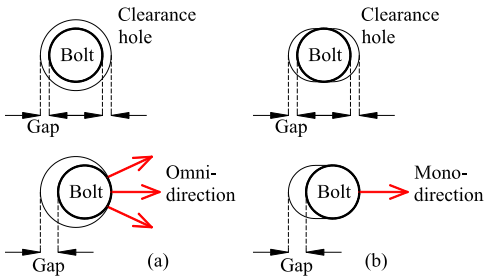

Fig. 5. Direction of bolt movement: (a) Oversized hole; (b) Slotted hole (Taib [28]).

During the movement of bolt shank, only friction force exists and its magnitude depends on the surface treatment of the plate and the bolt type. Friction force $F_{s,Rd}$ given by Eurocode 3 Part 1-8 [13] is expressed as follows:

$$F_{s,Rd} = 0.7k_s n\mu\sigma_{ub}A_s \quad (10)$$

where k_s is a coefficient to account for the effect of the type of bolt holes, n is the number of friction surface, μ is the coefficient of slip, A_s is the stressed area of bolt, usually taken as 75% of bolt gross area calculated using the nominal diameter.

A constant value equal to $F_{s,Rd}$ can be assumed as a threshold force before the bolt starts to sustain bearing stress.

d) Failure criteria

Failure of bolted connection is governed by its weakest component. Test results on fin plate connections subjected to catenary action [29, 32] indicate two possible failure modes, namely, shear failure of bolts and tear-out failure of steel plates, depending on the relative resistance between the bolts and the steel plates.

In component-based models, deformation capacity of each bolt row is defined in tension and compression respectively. Oosterhoof [31] provided the ultimate deformations of bolt rows in tension. The value is about 0.8 to 1.0 time of end distance. Since there are not sufficient test data on the ultimate deformations of bolt rows, it

is recommended that 70% of end distance can be used. For bolt rows in compression, shear failure of bolts is dominant over tear-out failure of fin plates, and the ultimate deformation is around 0.23 times of bolt diameter.

3.6. Vertical shear

An elastic spring can be used to model behaviour of joints subjected to shear force. In the vertical direction, bolts function in parallel. Therefore, stiffness of the elastic spring can be assumed to be the stiffness of bolts in bearing (k_i) multiplied by the number of bolts.

3.7. Strain rate effect

Material properties of steel and concrete can be affected by high strain rate, which leads to different behaviour of basic components under impact load. To consider the strain rate effect of steel and concrete materials, dynamic increase factors (*DIF*s) are used based on previous research studies [23, 33].

For concrete material, *DIF*s at strain rate $\dot{\varepsilon}_c$ from the *fib* Model Code [23] can be adopted.

For steel material, the Cowper and Symonds model is employed as follows:

$$DIF = 1 + (\frac{\dot{\varepsilon}}{C})^{\frac{1}{p}} \quad (11)$$

where 6844 and 3.91 are adopted for constants C and p [33]; $\dot{\varepsilon}$ is the strain rate.

Under impact loading scenario, the respective yield and ultimate strengths (σ_y and σ_u) of steel are modified by *DIF* obtained from Eq. (11).

The relationship between strain rate $\dot{\varepsilon}$ and displacement of each component Δ can be obtained from Eqs. (12) to (14), which are modified from the method by Stoddart et al. [34, 35].

$$\dot{\varepsilon} = \frac{\varepsilon}{\delta_t} \quad (12)$$

$$\delta_t = \frac{\Delta}{v} \quad (13)$$

$$\dot{\varepsilon} = \frac{\varepsilon}{\Delta} v \quad (14)$$

where v is the velocity and δ_t is the time to reach displacement Δ.

3.8. Model validation

To validate the modelling approach in Section 3.1, finite element (FE) package ABAQUS was chosen and the springs were simulated by *CONNECTOR* elements [36]. After determination of the spring properties, nonlinear springs were assembled in the beam-column joint. In the component-based model, beam element was used to simulate linear members including the column, beam, shear stud, circular hollow section (CHS) and bracket support. Shell element was used to simulate two dimensional members including the concrete slab and steel profiled sheeting. Rigid elements were used to connect the springs. Boundary conditions and loads were applied based on the test procedure.

Fig. 6(a) shows a comparison of load-versus-displacement curves from component-based model and experimental tests for specimen FP-static. Load applied to FP-static could be captured well by the simulation. When incorporating mechanical properties of beam flanges, load applied to W-static could also be captured well by simulations as shown in Fig. 6(b). Composite joints C75FP-M and C75W-M are shown in Figs. 6(c) and (d), respectively. Although the absolute values of applied load from models and test results have slight differences, each failure including fractures of fin plate, profiled sheeting, beam flanges and reinforcing bars could be captured well by the simulations.

Fig. 7(a) compares predicted displacements from the component-based model and the impact test for bare steel joint FP6-M530H3. Good agreement with the test result was achieved by simulations. In comparison, displacement from the component-based model for W-M830H3 (Fig. 7(b)) was slightly greater than that from the test result, indicating either the applied load was greater or stiffness of the model was smaller. The difference was small so that the component-based model was acceptable. For composite joint C75FP-M530H3 (Fig. 7(c)), displacement from the component-based model was only slightly smaller than that from the test result. Composite joint C75W-M770H3 had welded connections so that it was sufficient to withstand the impact load. Therefore, after attaining the peak displacement, C75W-M770H3 recovered partially as shown in Fig. 7(d). It is clear that good agreement with the test result was achieved although the peak displacement was slightly smaller, probably due to a stronger boundary condition. In the test, the A-frames and connected pinned supports acted as an elastic spring in the horizontal direction but due to gaps,

the restraint force may be overestimated by the simulation.

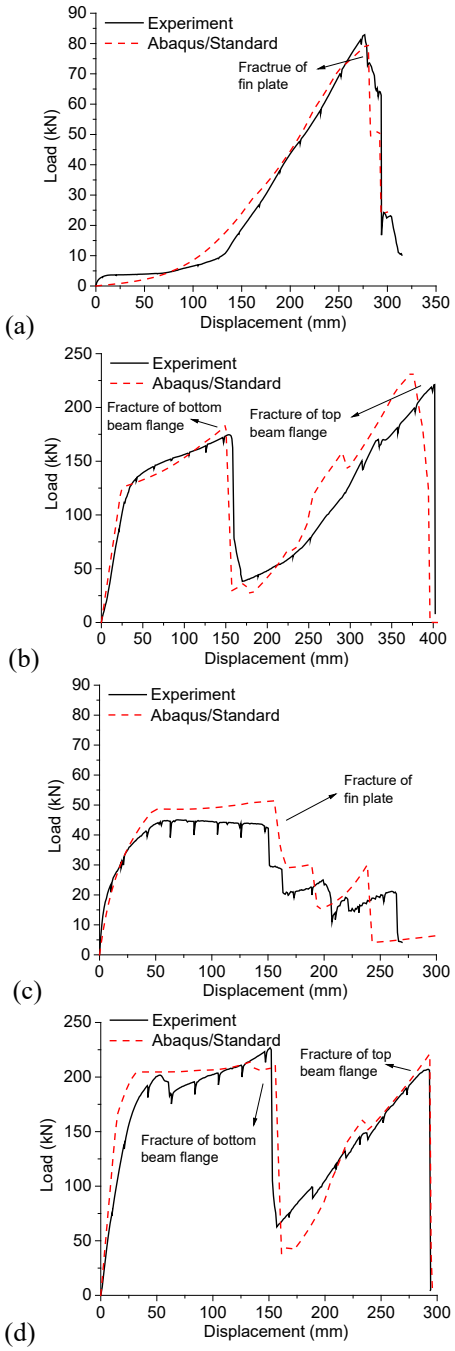

Fig. 6. Comparison of load-versus-displacement curves from component-based models and test results: (a) FP-static; (b) W-static; (c) C75FP-M; (d) C75W-M.

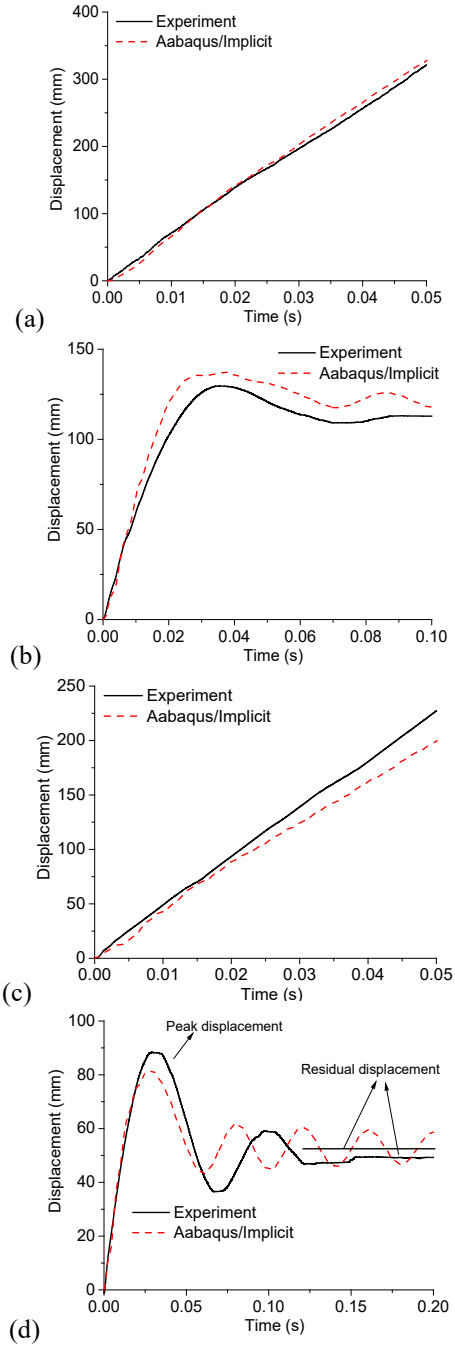

Fig. 7. Comparison of displacement-versus-time curves from component-based models and test results: (a) FP6-M530H3; (b) W-M830H3; (c) C75FP-M530H3; (d) C75W-M770H3.

4. Conclusions

Composite slab effect was beneficial to the initial load-resisting capacity of both FP and WUF-B joints subjected to quasi-static load. However, it induced a decrease of the load-resisting capacity of both types of joints at large deformation stage. Early loss of load-resisting capacity was induced as well due to demand of deformation capacity of beam-column connection at the initial stage.

Composite slab increased the mass and inertia of beam-column joints so that greater impact forces were observed in both FP and WUF-B joints compared to bare steel joints. Smaller displacements were observed due to the composite slab effect compared to bare steel joints.

A component-based modelling approach was proposed for steel and composite beam-column joints in this study. In the proposed component-based models, beam-column joints were discretised into individual springs, including the concrete slab, reinforcing bar, profiled sheeting, beam flange and bolted connection. Mechanical property of each spring was determined by material and geometry of individual component. Failure criteria were determined accordingly. Strain rate effect was considered through transforming strain rate to velocity of movement of each spring when applying the models to impact loading scenarios. The models were validated against typical quasi-static joint tests and impact joint tests. Good agreement was obtained.

References

[1] Thompson SL. Axial, Shear and Moment Interaction of Single Plate" Shear Tab" Connections. U.S.: Milwaukee School of Engineering; 2009.
[2] Driver RG, Oosterhof SA. Performance of Steel Shear Connections under Combined Moment, Shear, and Tension. Structures Congress 2012. Chicago, Illinois, U.S.2012. p. 146-57.
[3] Weigand J, Berman J. Integrity of Steel Single Plate Shear Connections Subjected to Simulated Column Removal. Journal of Structural Engineering. 2014;140:1-12.
[4] Cortés G, Liu J. Behavior of conventional and enhanced gravity connections subjected to column loss. Journal of Constructional Steel Research. 2017;133:475-84.
[5] Jamshidi A, Driver RG. Full-Scale Tests on Shear Connections of Composite Beams Under a Column Removal Scenario. Structures Congress 2014. Boston, Massachusetts, U.S.2014. p. 931-42.
[6] Karns JE, Houghton DL, Hall BE, Kim J, Lee K. Blast Testing of Steel Frame Assemblies to Assess the Implications of Connection Behavior on Progressive Collapse. Structures Congress 20062006. p. 1-10.
[7] Karns JE, Houghton DL, Hong J-K, Kim J. Behavior of Varied Steel Frame Connection Types Subjected to Air Blast, Debris Impact, and/or Post-Blast Progressive Collapse Load Conditions. Structures Congress 2009. Austin, Texas, U.S.2009. p. 1-10.
[8] Sadek F, Main J, Lew H, Bao Y. Testing and Analysis of Steel and Concrete Beam-Column Assemblies under a Column Removal Scenario. Journal of Structural Engineering. 2011;137:881-92.
[9] Sadek F, Main J, Lew H, El-Tawil S. Performance of Steel Moment Connections under a Column Removal Scenario. II: Analysis. Journal of Structural Engineering. 2013;139:108-19.
[10] Lew H, Main J, Robert S, Sadek F, Chiarito V. Performance of Steel Moment Connections under a Column Removal Scenario. I: Experiments. Journal of Structural Engineering. 2013;139:98-107.
[11] Li L, Wang W, Chen Y, Lu Y. Experimental investigation of beam-to-tubular column moment connections under column removal scenario. Journal of Constructional Steel Research. 2013;88:244-55.
[12] Li L, Wang W, Chen Y, Lu Y. Effect of beam web bolt arrangement on catenary behaviour of moment connections. Journal of Constructional Steel Research. 2015;104:22-36.
[13] BSI. Eurocode 3: Design of steel structures—Part 1-8: Design of joints. BS EN 1993-1-8. London, U.K.: British Standards Institution; 2005.
[14] BSI. Eurocode 4: Design of composite steel and concrete structures—Part 1-1: General rules and rules for buildings. BS EN 1994-1-1. London, U.K.: British Standards Institution; 2004.
[15] AISC. Specification for Structural Steel Buildings. ANSI/AISC 360-10. Chicago, Illinois., U.S.: American Institute of Steel Construction; 2010.
[16] AISC. Steel Conctruction Manual. AISC 325-11. Chicago, Illinois., U.S.: American Institute of Steel Construction; 2011.
[17] FEMA. Recommended seismic design criteria for new steel moment frame buildings. FEMA 350. Washington D. C., U.S.: Federal Emergency Management Agency; 2000.
[18] Yang B, Tan KH. Experimental tests of different types of bolted steel beam–column joints under a central-column-removal scenario. Engineering Structures. 2013a;54:112-30.
[19] Grimsmo EL, Clausen AH, Langseth M, Aalberg A. An experimental study of static and dynamic behaviour of bolted end-plate joints of steel. International Journal of Impact Engineering. 2015;85:132-45.
[20] Fujikake K, Li B, Soeun S. Impact response of reinforced concrete beam and its analytical evaluation. Journal of structural engineering. 2009;135:938-50.
[21] Yang B, Tan KH, Xiong G. Behaviour of composite beam–column joints under a middle-column-removal scenario: Component-based modelling. Journal of Constructional Steel Research. 2015;104:137-54.
[22] Kang S-B, Tan KH, Liu H-Y, Zhou X-H, Yang B. Effect of boundary conditions on the behaviour of composite frames against progressive collapse. Journal of Constructional Steel Research. 2017;138:150-67.

[23] fib. Model Code for Concrete Structures 2010. Berlin, Germany: John Wiley & Sons; 2013.
[24] CSA. Design of steel structures. CSA S16-09. Ontario, Canada L4W 5N6: Canadian Standards Association; 2009.
[25] Može P, Beg D. A complete study of bearing stress in single bolt connections. Journal of Constructional Steel Research. 2014;95:126-40.
[26] Rex CO, Easterling WS. Behavior and modeling of a single plate bearing on a single bolt. Blacksburg, V.A., U.S.: Virginia Polytechnic Institute and State University; 1996.
[27] Rex C, Easterling W. Behavior and Modeling of a Bolt Bearing on a Single Plate. Journal of Structural Engineering. 2003;129:792-800.
[28] Taib M. The Performance of Steel Framed Structures with Fin-plate Connections in Fire. U.K.: University of Sheffield; 2012.
[29] Weigand JM. The Integrity of Steel Gravity Framing System Connections Subjected to Column Removal Loading [Ph.D.]. U.S.: University of Washington; 2014.
[30] Koduru S, Driver R. Generalized Component-Based Model for Shear Tab Connections. Journal of Structural Engineering. 2014;140:1-10.
[31] Oosterhof SA, Driver RG. Shear connection modelling for column removal analysis. Journal of Constructional Steel Research. 2016;117:227-42.
[32] Yang B. The Behavior of Steel and Composite strctures under a Middle-Column-Removal Scenario [Ph.D.]. Singapore: Nanyang Technological University; 2013.
[33] Abramowicz W, Jones N. Dynamic axial crushing of square tubes. International Journal of Impact Engineering. 1984;2:179-208.
[34] Stoddart EP, Byfield MP, Davison JB, Tyas A. Strain rate dependent component based connection modelling for use in non-linear dynamic progressive collapse analysis. Engineering Structures. 2013;55:35-43.
[35] Stoddart E, Byfield M, Tyas A. Blast Modeling of Steel Frames with Simple Connections. Journal of Structural Engineering. 2014;140:1-11.
[36] Dassault Systèmes. ABAQUS 6.11 analysis user's manual2011.

12th International Conference on Advances in Steel-Concrete Composite Structures (ASCCS 2018)
Universitat Politècnica de València, València, Spain, June 27-29, 2018
Doi: http://dx.doi.org/10.4995/ASCCS2018.2018.7212

Fatigue of steel bridges

U. Kuhlmann[a]*, S. Bove[a], S. Breunig[a] and K. Drebenstedt[a]

[a]Institute of Structural Design, University of Stuttgart, Germany
*corresponding author, e-mail address: sekretariat@ke.uni-stuttgart.de

Abstract

Highway and railway bridges are exposed to cyclic stressing due to traffic loads and, therefore, have to be evaluated concerning fatigue. In most cases the fatigue evaluation is performed according to Eurocode 3 Part 1-9 on nominal stresses. To apply this nominal stress approach a detail catalogue is required classifying all relevant constructional details in terms of fatigue. Unfortunately, the existing detail catalogue of Eurocode 3 Part 1-9 reflects the state of the art of the 1990s and misses constructional details being important for today's bridge design. As an example the derivation of a new detail, the so-called lamellae joint, is presented. Furthermore, for two new types of innovative steel bridges, where Eurocode 3 Part 1-9 does not yet specify rules able to evaluate the characteristics of these bridges, research results are shown. These are the thick-plate trough bridges and truss bridges made of thick-walled circular hollow sections (CHS). The paper starts with an overview on the recent Eurocode developments, addressing more specific the fatigue verification according to EN 1993-1-9 and the statistical analysis of fatigue test data. In the following, information is given on the outcome of some recent research projects striving to extend the application range of Eurocode 3 Part 1-9. The final conclusion, in spite of all differences, show a common tendency.

Keywords: *Fatigue; Steel bridges; Eurocode 3 Part 1-9; Statistical analysis; Lamellae joint; Circular hollow section trusses; Thick-plate trough bridges.*

1. Introduction

Highway and railway bridges are exposed to cyclic stressing due to high traffic loads and, therefore, have to be evaluated concerning fatigue. In most cases the fatigue evaluation can be performed according to EN 1993-1-9 [1] on nominal stresses. To apply this nominal stress approach the detail catalogue, given by the Tables 8.1 to 8.10 in Eurocode 3 Part 1-9 and classifying a large spectrum of constructional details in terms of fatigue, has to be used. Unfortunately, this detail catalogue reflects the state of the art of the 1990s and misses constructional details being important for today's bridge.

As an example, the top or bottom flanges of steel and composite bridges consist in many cases of more than one plate welded on top of one another. In order to connect such stacks of steel plates on site, a so-called lamellae joint as visualized in Fig. 1 (c), can be used. However, this detail is not part of the basic standards like [1] or [2] and is not mentioned in the recommendations of the *International Institute of Welding*

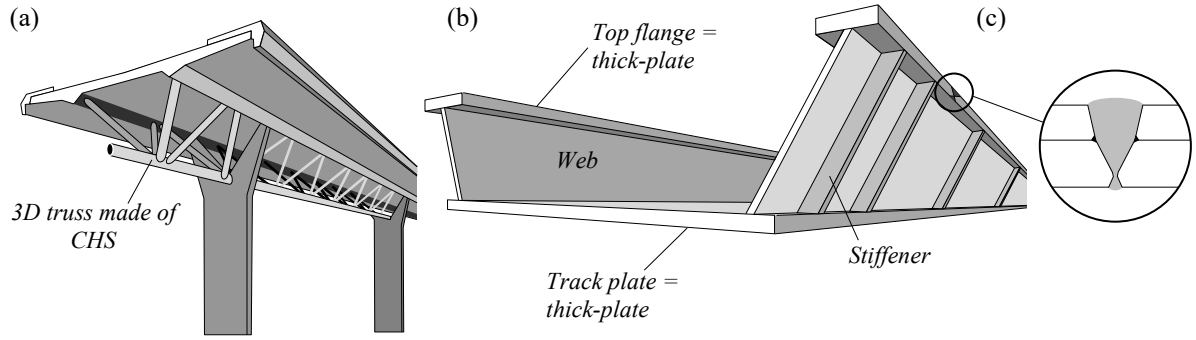

Fig. 1. (a) Example of a steel-concrete composite highway bridge, taken from [3], (b) example of a thick-plate trough bridge and (c) an example of a typical lamellae joint.

(IIW) [4]. As being built in practice, this detail is addressed in this paper based on recent research.

Thick-plate trough bridges represent another example of a structure not totally covered by the existing design rules, as some constructional details are subjected to a complex stress state which leads to a difficult identification of design relevant stresses, see Fig. 1 (b).

Furthermore, Eurocode 3 Part 1-9 does not specify rules for bridge structures not able to be evaluated by the nominal stress approach. An example of such structures are welded circular hollow section (CHS) joints with thick-walled chords (Fig. 1 (a)), as the Eurocode covers only two-dimensional K-joint geometries with wall thicknesses t_0 and $t_1 \leq 8$ mm. In addition, the design rules of CIDECT [5] and DNV [6] limit the chord slenderness to

$$\gamma = d_0 / (2 \cdot t_0) \geq 12 \text{ and } 8 \quad (1)$$

respectively, where d_0 is the chord diameter and t_0 is the chord wall thickness.

For this purpose this paper is firstly going to focus on the current state of standardization, especially of the Eurocode 3 Part 1-9, in order to give a short overview of the current work under coordination of the European Committee for Standardization (CEN). Subsequently, the statistical analysis of fatigue test data is addressed, as a statistical evaluation constitutes the key for the derivation of fatigue strengths. In a further step, the outcome of some recent German research projects striving to extend the application range of Eurocode 3 Part 1-9 is presented.

2. State of standardization – Eurocode 3 Part 1-9

The Eurocodes have become the primary standards for structural and geotechnical design in Europe. An overview for the planned revision of the Eurocodes is given in Fig. 2. At the moment the 2nd Generation of Eurocodes is under preparation. All existing Structural Eurocodes including EC 3: Design of steel structure - Part 1-9: Fatigue will be further developed under coordination by the European Committee for Standardization (CEN) [7].

The revision of the Eurocodes comprises two phases. The first part focuses on general revision and maintenance of the Eurocodes. The code revision is launched in form of a call for 'systematic reviews' to the national standardizing bodies. The suggestions and comments that are given in the systematic review will be evaluated and incorporated by CEN Subcommittees and Working Groups. The second main activity in the frame of the Eurocode revision cares about further evolution with focuses on new methods, new materials and new regulatory and market requirements. It is realized in the frame of the mandate M/515 [8], which was agreed in December 2012 between the European Commission and CEN. The final realization is conducted by so called Project Teams (PT) that consist of a maximum of six experts [8].

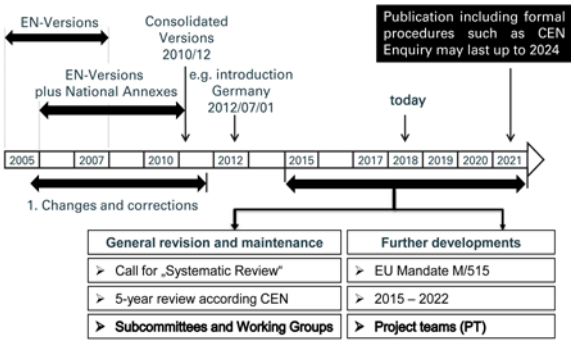

Fig. 2. Planned time-table for the revision of the Eurocodes.

The revision of EN 1993 Part 1-9 focuses mainly on a more user-friendly formulation and improved wording of the existing design rules. The practical application on Eurocode 3 Part 1-9 since 2005 and the systematic review of the standard in 2017 has identified a couple of unclear or ambiguous rules that require technical clarification. For example, the requirements on the fabrication in the fatigue detail catalogue in Sec. 8 of [1] are formulated too unclear and leave room for interpretation. A revision of the tables aims to clarify the figures and descriptions of the constructional details. The requirements on the fabrication of welded details will be clarified with help of an additional column that shows weld symbols. An example is given in Fig. 3. It shows a butt weld that is stressed in longitudinal direction. The symbol shows that a root backing is needed. Information regarding the fabrication of a fatigue loaded constructional detail are important, because their influence could be significant for the fatigue strength.

Detail category	Constructional detail	Symbol
100	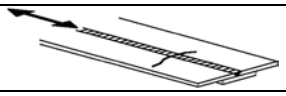	

Fig. 3. Additional weld symbols.

In future the fatigue detail catalogue in EN 1993-1-9 will be complemented by new constructional details, which are required in practice. For example, the lamellae joint will be introduced, see Chapter 4.

3. Statistical Analysis of Fatigue Test Data

3.1. Background

The core of Eurocode 3 Part 1-9 is the fatigue assessment by using the corresponding fatigue detail category that is defined in the standard. The detail category defines the underlying S-N curve, which is characterized by the reference value, $\Delta\sigma_C$, and the slope, m, of the *S-N* curve. The curves are based on experimental data. In order to guarantee a uniform safety level, the fatigue strength of Eurocode 3 expressed by its characteristic reference value $\Delta\sigma_C$ for $2 \cdot 10^6$ stress cycles should be derived on the basis of standardized and commonly agreed criteria. Because of its scatter, there is a need for statistical analysis of the test data to define reliable values $\Delta\sigma_C$. However, in practice the values $\Delta\sigma_C$ are derived in different ways, which limit their comparability [9].

3.2. Regression Analysis

Generally, test data in the high cycle fatigue range (finite life) are allocated to a curve defining a linear relationship between the numbers of stress cycles to failure, N, and the applied stress ranges, S, according to *Basquin* [10] on a log-log scale using the least-square method. A so obtained *S-N* curve defines the 50%-survival probability of the considered sample and has to be transformed into a characteristic *S-N* curve for design purposes by statistical analysis.

In the frame of fatigue testing the stress level S is normally predetermined, therefore it is an independent variable. Contrarily, the number of stress cycles to failure N are dependent (on the stress level). According to *Basquin* [10] there is a linear relationship between log S and log N with decimal logarithm (base 10), see Eq. (2).

$$\log N = \log a - m \cdot \log S \qquad (2)$$

where log N = logarithm (base 10) of corresponding number of cycles to failure N; log a = intercept on the log N axis; m = negative inverse of the mathematical slope of *S-N* curve; log S = logarithm (base 10) of allowable stress range S.

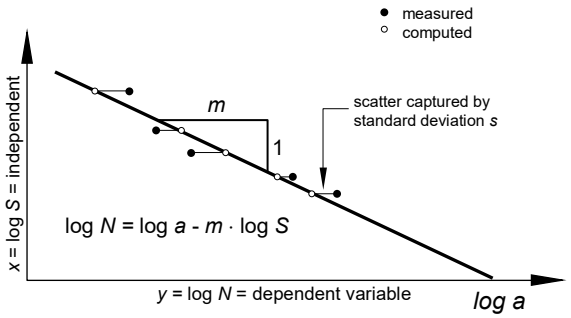

Fig. 4. Linear regression of *S-N* curve.

Due to the scatter, there is a statistical uncertainty in the variables log a and m. These unknown model parameters are estimated from the fatigue data. If the slope of the *S-N* curve is already known due to existing information, only log a has to be determined. The result forms an average *S-N* curve representing the 50 % survival probability of the tested data set or rather of the sample, see Fig. 4.

3.3. Statistical Evaluation

There is a tendency for errors that occur in many real situations to be normally distributed. The normal distribution is also referred to as the Gaussian distribution. It can be shown graphically by a typical Gaussian bell curve, see Fig. *5*.

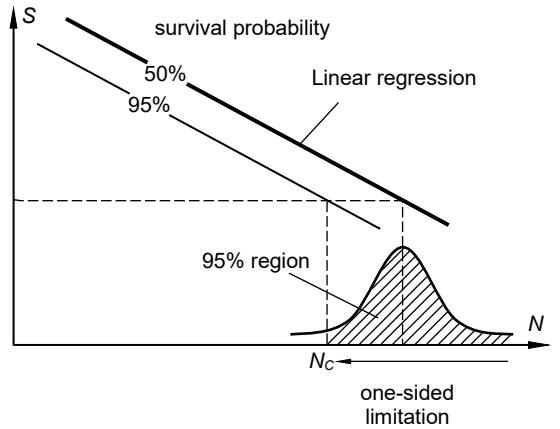

Fig. 5. Gaussian bell curve with one sided limitation.

The normal distribution is defined by only two parameters: mean value and standard deviation, s. Is the sample sufficiently large to represent the whole population, the characteristic *S-N* curve

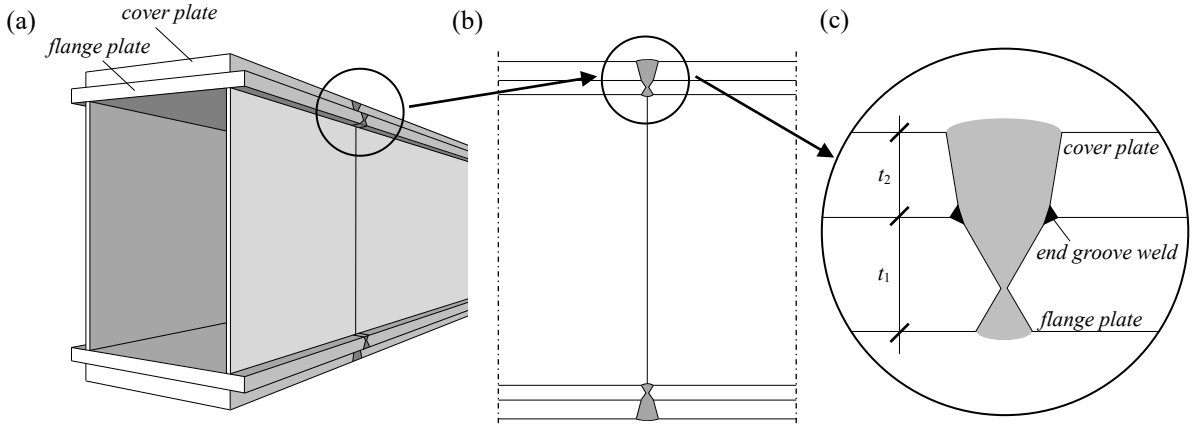

Fig. 6. Welding detail lamellae joint: (a) and (b) overview, (c) detail.

with 95 % probability of survival could be calculated with help of the corresponding fractile value of the normal distribution. EN 1990 [11] recommends at least 100 specimens to represent the whole population. Otherwise the statistical uncertainty associated with the number of tests should be taken into account. The so called prediction interval is an appropriate method to do so. A prediction interval is an estimate of an interval, in which m future observations are expected to fall in with a certain probability. It defines on the basis of the sample and under consideration of the statistical uncertainty, information about the scatter of fatigue resistance for a future structure. The prediction interval is using the *t*-distribution instead of the Gaussian distribution. It is defined by an additional third parameter: the degree of freedom. It takes into account the sample size and the amount of parameters with a statistical uncertainty. In case the degree of freedom becomes large, the shape of the distribution fits to the Gaussian bell curve. The coefficient *t* of Student's *t* distribution is tabulated in common literature, for example by *Wadsworth* [12].

Another possibility for statistical analysis is given in the Eurocode 0 [11]. The standard defines, among others, rules for design that is assisted by testing. The corresponding chapter in Eurocode 0, Annex D gives information about statistical determination. In case that there is only one parameter that is afflicted with a statistical uncertainty, Eurocode 0 and the prediction interval are giving identical results [9].

3.4. Summary

The derivation of a characteristic *S*-*N* curve should take into account the scatter of test data, statistical uncertainty associated with the number of tests and prior statistical knowledge. The prediction interval delivers a closed mathematical solution that is suitable for application in the frame of statistical analysis of fatigue data for constructional details in steel construction.

4. Introduction of a new constructional detail: the lamellae joint

4.1. Background

Plated steel girders are quite common in steel and composite bridge design. In consideration of the economic aspects, it is useful to vary the cross sections of the flanges by cover plates. The adaption of the flanges to the internal forces can be put into practice in two different ways. Either by using flanges with varying thickness or by using cover plates (lamellae) which are welded to the flange plate.

Due to restricted transport length and assembly weight, it is commonly necessary to implement in-situ joints in the girder that are called lamellae joints. In contrast to a common butt joint, the so-called end groove weld is characteristic for the lamellae joint and influences the joint´s fatigue behavior, see Fig. 6.

The lamellae joint has been an important constructional detail in German bridge design since 1935. Therefore, in old German regulations such as DS 804 [13] and TGL 16500 [14] the lamellae joint was part of the fatigue detail catalogue. However, up to now the lamellae joint is missing in the fatigue detail catalogue of Eurocode 3 Part 1-9 [1].

4.2. Experimental investigations

A research project (DASt/IGF No. 15380) [15] realized by University of Stuttgart, Institute of Structural Design, investigated the size effect of the fatigue behavior of lamellae joints in detail including experimental investigations. Lamellae joints comprising two plates, according to Fig. 6 were tested. One primary goal of the research project was to identify whether the size effect depends on the maximum plate thickness of single plates connected by the lamellae joint or on the overall thickness of the joint.

In the follow-on research project (DASt/IGF No. 17104) [16] a larger range of parameters was investigated in an extensive test program.

There were four different test series. The plate thickness in these series included the application range common for bridge design. In test series No. 100 a pronounced size effect was expected. In contrast, it was expected that there is no size effect in test series No. 200 because of the thin single plates. The plate thickness of test series No. 300 was chosen between the two other series. The plate thickness ratio of the test series No. 100, 200 and 300 amounts to 0.8. To investigate the influence of a different plate thickness ratio, an additional test series No. 400 was carried out having a ratio of 0.5. Table 1 gives an overview of the test series.

Table 1. Fatigue tests on lamellae joints, from [15] and [16].

Objective	***Size effect***			***Plate thickness ratio***
Test-series	**100**	**200**	**300**	**400**
t_1 [mm]	80	20	40	25
t_2 [mm]	100	25	50	50
t_1 / t_2	0.8	0.8	0.8	0.5
No. of specimens	15	10	15	10

4.3. Test results

The fatigue strength is directly linked with the stress concentration of the critical notches of the constructional detail's geometry. The investigations have shown three different types of critical notches, see Fig. 7.

- **Notch #1**: weld toe from surface layer of the thinner plate (t_1)
- **Notch #2**: weld toe from surface layer of the thicker plate (t_2)
- **Notch #3**: root run of the end groove weld

As observed during the fatigue tests, there are three potential modes of failure of the lamellae joint. The modes differ by various crack initiation points. The cracks can start at the weld toe (notch #1 or #2), but a crack initiation at the end groove weld (notch #3) is also possible.

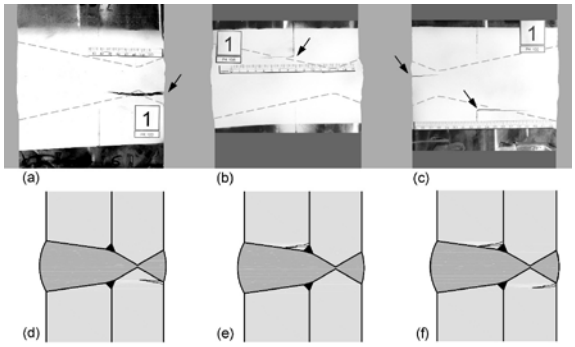

Fig. 7. Failure of the specimens No. (a) 103, (b) 106, (c) 102; (d) Crack starting from weld toe, (e) Crack starting from the end groove weld, (f) mixed crack mode.

Fig. 8 shows the failure of specimen No.109 with crack initiation at the weld toe.

Investigations on cracked specimens have shown that a discontinuity in the end groove weld is not necessarily an initiation point for the fatigue crack. Thus, the test results imply common irregularities in the root of weld.

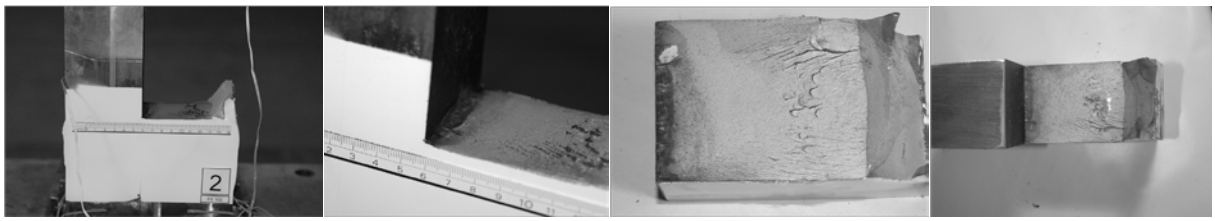

Fig. 8. Failure of the specimens.

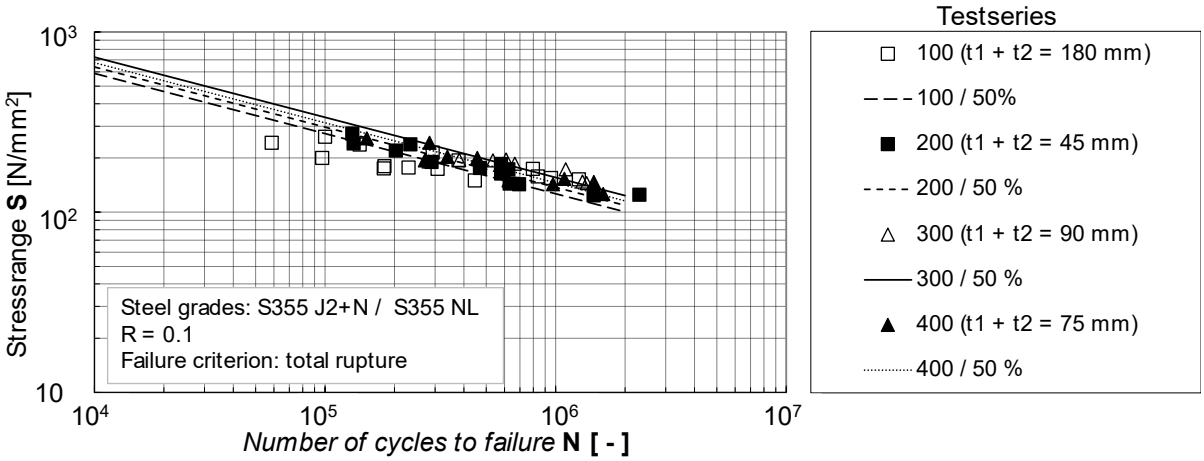

Fig. 9. Test results with 50 % S-N curves.

4.4. Statistical evaluation of test results

First, the series were evaluated individually by a linear regression analysis, see Fig. 9. A constant value of $m = 3$ has been assumed. Comparing the results of the different series in Fig. 9 it turns out, that the results of series 100 with high overall thickness of 180 mm are below the other results. This indicates that the fatigue strength of the specimens depends on the overall joint thickness.

According to Eurocode 3 Part-1-9 the size effect due to thickness should be taken into account as given in Eq. (3):

$$\Delta\sigma_{C,red} = k_s \cdot \Delta\sigma_C \tag{3}$$

where $\Delta\sigma_{C,red}$ is the reduced reference value of the fatigue strength; k_s is the reduction factor for fatigue stress to account for size effect; $\Delta\sigma_C$ is the reference value of the fatigue strength at $N_c = 2$ million cycles.

For plate packages with t > 25 mm the reduction factor is calculated as given in Eq. (4):

$$k_s = \left(\frac{25}{t}\right)^n \tag{4}$$

where t is the overall thickness of all plates and n is the correction exponent. The correction exponent n, could be determined on experimental basis by searching for the lowest standard deviation s, of the scatter.

For a conservative estimate, the value is set to $n = 0.2$. This is equal to the value for the thickness correction exponent for butt joints in Eurocode 3 Part 1-9.

Fig. 10 shows the nominal stress range transferred to 2 million cycles and scaled to reference thickness $t_{ref} = 25$ mm. The detail category of the overall statistical evaluation, based on the prediction interval, indicates a detail category 104. Nevertheless, it is proposed to apply detail category 90 for the constructional detail of the lamellae joint in the frame of Eurocode design. This detail category is equal to detail ⑤ in Eurocode 3 Part 1-9, Table 8.3: Transverse butt welds. Fig. 11 shows a proposal to apply the constructional

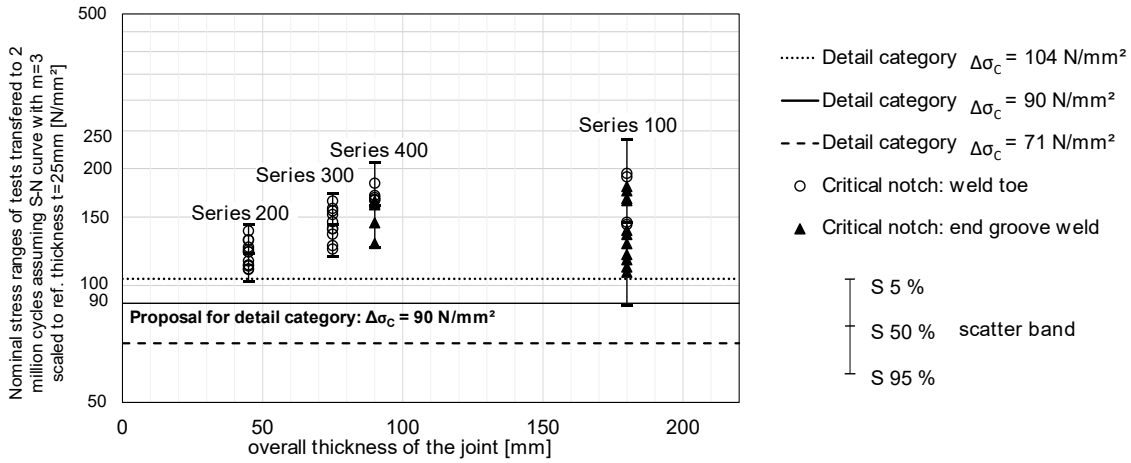

Fig. 10. Test results: proposal for detail category.

detail of the lamellae joint in the frame of Eurocode design, [17].

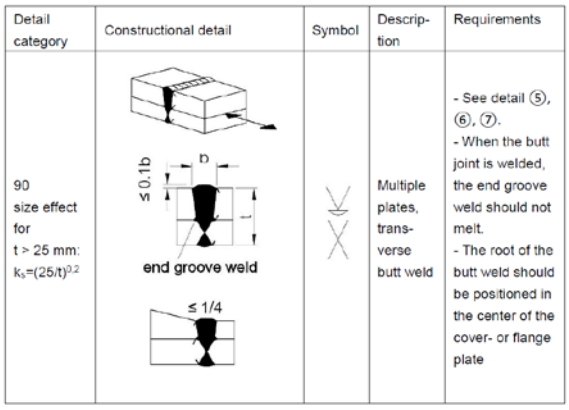

Fig. 11. Proposed change: additional row in Table 8.3: transverse butt weld.

5. Developments and fatigue behavior of short span railway steel bridges as thick-plate trough bridge

5.1. Introduction

One promising steel bridge solution for railway bridges of small spans is the thick-plate trough bridge. The steady improvement of fabrication processes and welding properties in the steel plate production led to an innovative design of cross sections for short span railway bridges. With steel plates of thicknesses from around 80 to 120 mm, the so-called thick-plate trough bridges came up around 20 to 25 years ago.

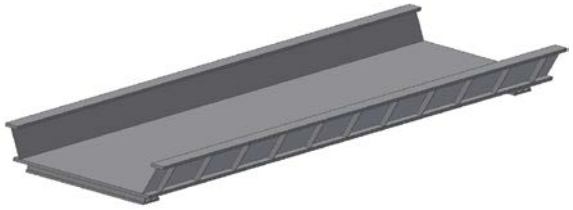

Fig. 12. Isometric view of thick-plate trough bridge [18].

An isometric illustration of the thick-plate trough bridge is given in Fig. 1(b) and Fig. 12, clearly showing the improvement in construction height because no transverse girders are necessary. In order to save thick-plate material the webs are not perpendicular, but declined fillet welded to the bottom plate.

This type of construction is especially interesting for the replacement of railway constructions in inner city areas, where a change of the rail track is restricted especially in height because of the conditions of the existing structure. Another advantage is the simple erection due to the possibility to prefabricate the whole steel superstructure and erect it by crane lifting in one piece.

5.2. Project overview and motivation

In the frame of the German cooperative FOSTA-AiF research project called 'Holistic Assessment of Steel- and Composite Railway Bridges according to Criteria of Sustainability' [18], three different railway bridge types were evaluated in terms of sustainability. Therefore, three typical bridges for different application fields were chosen and were compared to variants in view of economical, ecological and socio-functional aspects, see [18] and [19].

Among the three bridge types, the thick-plate trough bridge was chosen as steel bridge solution for railway bridges of small spans. When it comes to the economical, ecological and socio-functional assessment of a bridge, the durability of the construction plays an important role. The durability of a steel bridge construction and thus its sustainability is mainly affected by corrosion processes and fatigue phenomena. Especially for heavy loaded railway bridges the fatigue assessment is defining the design.

Within the project [18], the thick-plate trough bridge was investigated in terms of construction and design, especially regarding the fatigue behavior. In the following, the latest findings of [18] and [20] concerning the fatigue behavior of thick-plate trough bridges are summarized.

5.3. Load distribution

For this type of bridge, the thick-plate deck unifies the function of the bottom flange of the main girder as well as the track plate. Transverse girders become dispensable, as the up to 100 mm thick plate transfers the direct loading to the main girders. This effect, which can be seen in Fig. 13, leads to a large deflection of the bottom plate in vertical direction, with a maximum in the center of the bridge, under load model 71 (LM71), the nominal load model for normal railway tracks according to EN 1991-2 [21].

As a consequence of the clamping of the web to the stiff thick-plate, a bending moment occurs

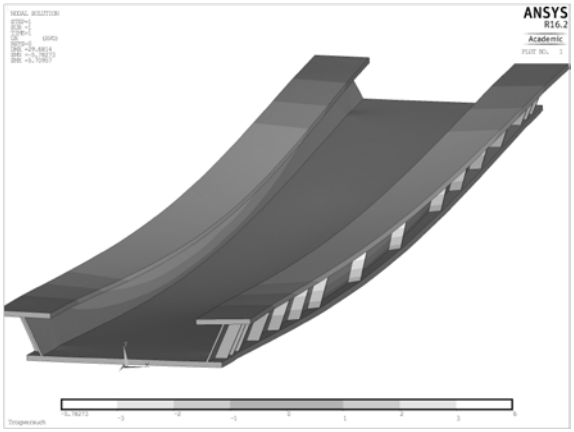

Fig. 13. Sum of deformations of thick-plate trough bridge [20].

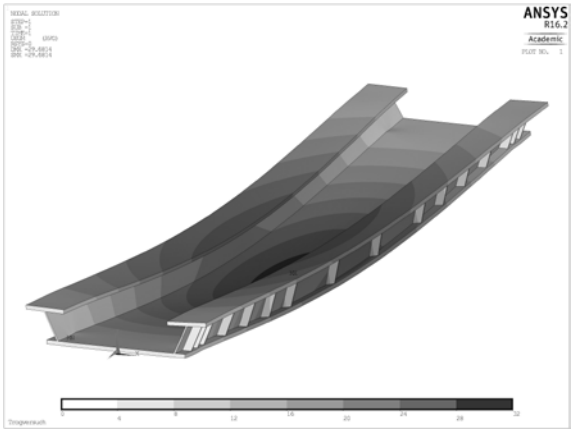

Fig. 14. Horizontal deformations of thick-plate trough bridge [20].

around the thickness of the web. This transversal bending of the web has to be transferred by the double fillet welds connecting the web to the bottom thick-plate. This is illustrated in Fig. 14, where the horizontal deformations of the trough bridge as a result of LM71 loading is given.

Therefore, the double fillet weld is loaded by direct stresses from the global bending moment respectively the resulting shear action of the bending moment of the main girder as well as this transversal bending moment resulting from the transverse frame action of web and thick plate.

Fig. 14 gives the horizontal deformations in an elastic FE-Analysis, clearly showing that the upper flanges with the webs tend to come to the middle of the bridge.

The effect of transversal bending even increases for the T-section, where the main girder is supported by a transverse stiffener. This transversal bending of the fillet weld is mostly neglected in the design process. Lateral torsional buckling of the main girders is prevented by a high number of transverse stiffeners, supporting the webs and connected to the upper flanges of the main girders and the bottom thick-plate.

Following the aim of [18] to improve this bridge structure, save fabrication costs and maintenance time and costs, the number of transverse stiffeners may be reduced, however the effects of transversal bending would be increased.

Previous investigations from *Schrade* [22] on different thick-plate bridges have shown that the deflection of this bridge type can be estimated with the help of the analytical method of the Generalized Beam Theory, also see [23]. Since this method is applicable for prismatic cross sections considering the distortion of the cross-section, the results revealed that there is a significant bending moment at the location of the connection of the double fillet welds between web and thick-plate. Especially, when it comes to the fatigue assessment this welded connection represents a sharp notch.

This is why *Schrade* [22] recommends butt welds instead of fillet welds connecting the web

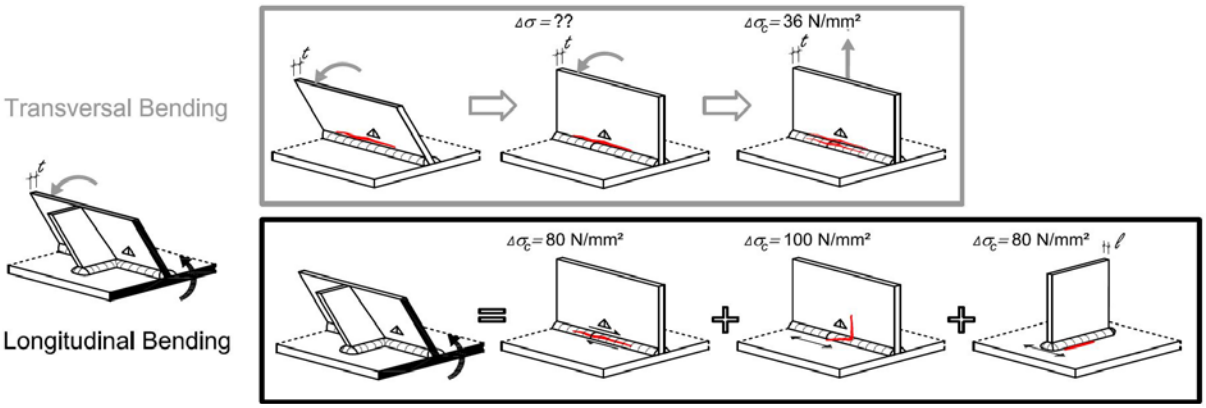

Fig. 15. Categorisation of longitudinal bending and transversal bending from [20] in weld detail categories of EN 1993-1-9.

to the upper and the bottom flange. Furthermore, in [22] a web plate thickness of 40 mm is recommended, whereas the common practice is a web plate thickness of 30 mm. So the question arises if this transversal bending at the connection is purely theoretical and minimal or real and measureable, and thus may be decisive.

5.4. Fatigue behavior

When it comes to the fatigue design according to EN 1993-2 [2] and EN 1993-1-9 [1], using the nominal stress approach, several fatigue details have to be considered individually to enable the comparison with the detail categories given in the tables in EN 1993-1-9.

Therefore, a consideration according to the directions of internal forces can be useful. As can be seen from Fig. 15, where a half of the main girder with a transverse stiffener is cut out, there is longitudinal bending and transversal bending for two different "T-sections". Trying to assess these details due to the existing fatigue details according to EN 1993-1-9 [1] one has to further differentiate.

Identifying the single welded details according to the detail catalogue in EN 1993-1-9 one question occurs: for transversal bending of a double fillet weld, no detail category exists. Thus, to cover this effect on the safe side, the detail of the tensioned T-stub with fillet welds (see Table 8.5 Detail 3, in [1]) is usually chosen, which is the lowest detail category in EN 1993-1-9 with a fatigue resistance of only 36 N/mm².

In addition, the constructional details of the transverse stiffener welded to the bottom thick-plate, see Fig. 15, and the longitudinal fillet weld under shear welded to the tension flange (the thick-plate), see Fig. 15, have to be considered.

The complex stress state at the bottom plate in combination with the accumulation of welded details and the additional effects of transversal bending led to the necessity of experimental and numerical investigations for the fatigue design of this innovative type of trough bridge.

5.5. Test results on double fillet welds under web plate bending

Within two series of small scale tests with differing plate thicknesses (series 100 and series 200) the fatigue resistance of the transversally bended longitudinal fillet welds could be investigated, see Fig. 16. By using a configuration of a thick-plate of 100 mm and a web plate thicknesses of 30 mm (Series 200) a significant scale effect was detected, compared to Series 100 with 30 mm track plate dimension and 10 mm web plate thickness.

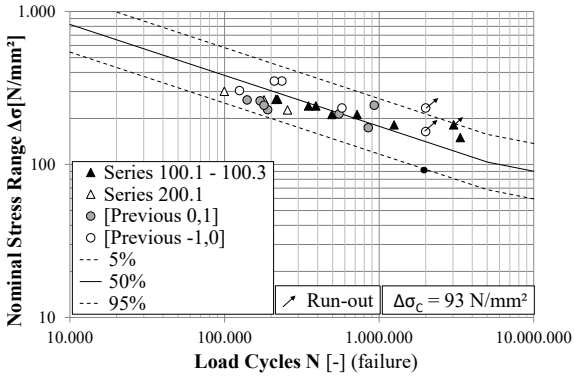

Fig. 16. Results of small scale tests under transversal plate bending (with size effect correction).

Previous fatigue test results from investigations on slender bridge webs from *Guenther et al.* [24] and bended crane girder webs of *Kuhlmann et al.* [25] could be used in addition to the current results to determine a fatigue resistance for transversally bended fillet welds. The evaluation leads to a fatigue resistance $\Delta\sigma_C$ of around 90 N/mm².

Besides that, a rule concerning the scale effect for the plate thicknesses larger than 25mm were proposed. The investigations also showed a clear improvement of the fatigue resistance by the application of High Frequency Mechanical Impact Treatment (HFMI).

Detailed information on the small scale tests and results can be taken from [26].

5.6. Trough test program and execution

In order to investigate the complex stress state of thick-plate trough bridges considering the transversal bending effects, large scale trough bridge tests were planned, as realistically as possible. Therefore, drawings of existing thick-plate trough bridges have been provided by DB Netz AG and advisory project partners. The selected bridges have been evaluated in order to define the most relevant and thus realistic proportions of a typical thick-plate trough bridge. Consequently, the trough bridge specimens also reflected the residual stress state of such a real bridge.

In addition, the post-weld treatment method High Frequency Mechanical Impact (HFMI)

treatment has been applied in order to examine the possible improvement in view of fatigue strength for a real bridge structure.

The test program consisted of four small trough bridges, scaled from real bridges in a ratio of 1:3, with slight simplifications at the supports. As the test specimens were manufactured by four different steel construction companies, it was decided to apply HFMI-treatment only on one side of each test bridge to be able to compare the treated main girder to an untreated girder at the other side produced by the same fabricator.

The tests were executed at the Materials Testing Institute of the University of Stuttgart (MPA) with a portal frame on a testing field with two 1.000 kN hydraulic cylinders applying compression force with a stress ratio of R = 0.1.

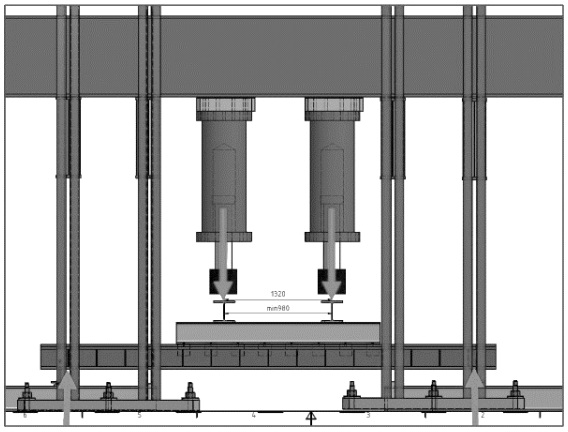

Fig. 17. Longitudinal view of test setup of trough tests.

In order to have realistic load behavior, the load introduction was realized with a downscaled ballast bed with typical railway gravel. Furthermore, downscaled railway sleepers and tracks were used to distribute the load of the two cylinders.

Fig. 17 shows the test-setup in the longitudinal view. Each test bridge was supported at four points. At all of these points the test bridge was enabled to move freely in plane. Hinged bearings were realized to avoid constraints, since the test setup defines the load introduction to be fixed points.

5.7. Results

The crack detection after and during the test was done with the help of the monitored strain gauges at chosen locations and with non-destructive testing such as fluorescent magnetic particle testing and dye penetration testing, where access was possible. Since the inner side of the test bridge was filled with gravel for load distribution, it could be visualized only after the execution of the test.

The detected cracks mainly fell into two categories, the ones that led to global failure of the specimens and the ones that occurred, but were not dominant and did not harm the loading capacity of the whole test specimen.

With the help of strain gauges applied on the web, close to the fillet weld, and non-destructive crack testing it could be shown that the phenomenon of transversal bending of the web plates and welds exists. Especially at the inner side of the bridge on the longitudinal fillet welds, cracks appeared along the middle of the weld or at the weld toe in longitudinal direction, see Fig. 18. The location of these longitudinal cracks is mainly at the inner fillet weld, where the transverse stiffener and the web acts as a stiff T-section. It can be excluded that these cracks resulted of shear stresses, since they appeared at locations with low global shear stress. This is why those cracks seemed to be bending-induced. However, these cracks did not lead to a significant failure mode.

Fig. 18. Crack arising at inner side longitudinal weld of trough tests.

The failure cracks, which led to the global failure of the bridge were cracks rising across the longitudinal double fillet welds between the web and bottom flange. These cracks occurred in three of four cases at the untreated girder close to the stiffener, in the area of the girder where global shear and longitudinal stresses superimpose maximal, these points are marked with red circles in Fig. 19.

Para seguir leyendo haga click aquí